A *Plasmodium falciparum* molecular mechanism of heme binding and sensitivity to artemisinins.

Smritikana Dutta[1], Mohammad Faaiz[1], Saikat Bhattacharjee[2], Kasturi Haldar[3,*] and Souvik Bhattacharjee[1,*]

[1] Special Centre for Molecular Medicine, Jawaharlal Nehru University, New Delhi 110067. India.

[2] Regional Center for Biotechnology, 3rd Milestone, Faridabad-Gurgaon Expressway, Faridabad, Haryana 121001. India.

[3] Department of Biological Sciences, University of Notre Dame, Notre Dame, Indiana, IN 46556, USA.

[*] Corresponding authors

Corresponding authors address:

souvik@jnu.ac.in . Special Centre for Molecular Medicine, Jawaharlal Nehru University, New Delhi 110067. India.

khaldar@nd.edu. Department of Biological Sciences, University of Notre Dame, Notre Dame, Indiana, IN 46556, USA.

Abstract

Heme is critical to activating artemisinins (ARTs), drugs essential for malaria control. *Plasmodium falciparum* malaria Kelch13 (K13) binds heme *in vitro,* but the consequences for *in vivo* functions remain unknown. As taut regulation of free-heme levels is not feasible in infected erythrocytes, we developed human Du145 cells as a model to study molecular properties of K13 at biological heme concentrations. We show that K13 levels are exquisitely responsive to nanomolar amounts of heme. Heme stabilizes K13 with molecular specificity, raises its oxidative-stress responses and association with autophagic-endosomes. Targeted disruption of lysosomal autophagy further increases K13 levels to fuel ART-induced redox-cell death that is proportional to K13 intensities at physiological heme levels. K13's kelch-domain confers both heme and ART responsiveness to its mammalian orthologue KEAP1. These data suggest a novel molecular mechanism of K13-heme binding regulating ART-sensitization and power of models to study frontiers of pro-oxidant stress.

30 **Introduction**

31 Artemisinins (ARTs) are highly effective in curing blood-stage infection of *Plasmodium falciparum,* the
32 deadliest of human malaria parasites[1]. These drugs are critical components of artemisinin-based
33 combination therapies (ACT) that have played a key role in reducing the global burden of malaria and
34 remain the cornerstone of its control worldwide[2]. Heme increases their potency because it cleaves
35 the ART-endoperoxide bridge yielding highly reactive oxy-centered and C4-centered radicals[3] that
36 alkylates a wide range of cellular components causing oxidative damage, which results in parasite cell
37 death[4,5]. When malaria parasites infect red blood cells, they digest the host hemoglobin to actively
38 produce heme in the parasite's food vacuole (FV). High levels of heme are presumed to confer the
39 exquisite sensitivity of ARTs in killing malaria parasites[6], although whether other parasite factors
40 potentiate heme activity remains unknown[7].

41 Despite the prevalent model that ART kills through indiscriminate alkylation and damage of parasite
42 lipids, proteins and DNA[8–10], robust clinical resistance has been ascribed to one major gene *Pfkelch13*
43 (K13; PlasmoDB ID: PF3D7_1343700)[11], which has been shown to be causal for resistance[12].
44 Artemisinin resistance (ART-R) poses a significant threat to malaria control[13,14]. Consequently, K13
45 has been intensely studied over the last decade[15–19]. The consensus data suggest that it is a
46 cytoplasmically synthesized protein associated with vesicular structures, including the parasite's
47 digestive endosomes, apicoplast, mitochondria, endoplasmic reticulum as well as vesicles enriched in
48 Rabs, ATG18 and phosphatidylinositol 3-phosphate (PI3P)[9–11]. At the parasite's trophozoite stage,
49 when hemoglobin uptake and digestion are most active, K13 regulates endocytosis *via* structures
50 called cytostomes, and resistance mutations suppress this process[20,21]. But notably, these very
51 trophozoite stages remain highly susceptible to ARTs in K13 mutant parasites, suggesting that while
52 the process of hemoglobin uptake maybe regulated by K13, it may not be the major target of
53 resistance.

54 We have recently reported that recombinant and parasite-derived K13 directly bind molecular heme
55 with a dissociation constant (K_d) of 61.5 nM[22]. Heme binds to many proteins[23,24]. This includes
56 albumins with a K_d range of 2-40 μM[25], explaining their ready capacity to transfer heme to wide range
57 of acceptors[26]. In contrast heme-oxygenases which degrade heme, bind it with nanomolar (3-300
58 nM) affinity[27]. This suggests that with a K_d of 61.5 nM, K13 engages in at least moderately tight heme-

59 binding. Heme binding is known to effect profound structural changes in proteins[28] and heme is
60 implicated in oxidative stress metabolism[29]. However, the consequences of heme binding for K13's
61 stability and turnover, and whether heme-binding induces K13-mediated redox-controlled responses
62 remain entirely unknown. Furthermore, K13's engagement of antioxidant and detoxification systems,
63 as regulated by its closest mammalian orthologue Kelch-like ECH-associated protein 1
64 (KEAP1)[11,30,31], is also unstudied. Finally, whether and how heme, bound with significant affinity to
65 K13, is dislodged and the associated implications for mechanisms of ART-based killing remain to be
66 discovered.

67 Since *in vitro* studies suggest that K13 binds heme with a K_d of 61.5 nM[22], regulation of associated
68 cellular mechanisms may be expected to be initiated at nanomolar to low micromolar concentrations.
69 However, carefully controlling heme levels in this range remains unfeasible in blood-stage parasites.
70 This is because the host erythrocyte contains high levels of hemoglobin (3.2-3.6 mM)[32], whose
71 digestion is a major source of parasite heme. Erythrocytes also contain high levels (21 ± 2 μM) of free
72 heme[33] which may translocate through passive and facilitated pathways[24,34]. Since mature human red
73 cells are enucleated and terminally differentiated, these host sources of heme cannot be genetically
74 'turned off' post infection. Moreover, their reduction compromises parasite health[35]. Genetic or
75 chemical targeting of parasite's *de novo* heme biosynthesis in infected erythrocytes appears to have
76 no effect on parasite growth[36,37], suggesting that heme provided by exogenous pathways can be
77 supplemented from host-derived sources. Notably, free heme levels in most non-erythroid cells are in
78 the nanomolar range (25-300 nM)[34], but in *P. falciparum* they are reported to be considerably higher
79 (at 1-2 μM or higher)[38,39], suggesting that throughout blood-stage infection the parasite may reside in
80 a high intracellular heme environment.

81 We desired a cell system to study the molecular functions of K13 and their regulations by nanomolar
82 concentrations of heme. We therefore used a model non-erythroid mammalian cell line Du145[40] with
83 reduced levels of KEAP1, adapted to grow in heme-depleted media, and whose free heme levels
84 were tightly regulable by blocking endogenous heme biosynthetic enzymes. These Du145 cells were
85 otherwise capable of an active redox response[41]. Our goal was to query whether K13 and heme
86 engaged protective responses against oxidative stress, as well as obtain mechanistic understanding

87 of how K13, heme or both components triggered sensitization of cells to killing by ARTs. The lessons
88 learned maybe applicable across a broad range of cellular systems.

89 **Results**

90 **Heme increases cellular levels of K13 through binding and stabilization**

91 Human Du145 cells (HTB-81, ATCC, *www.atcc.org*) contain a full length wild-type *Keap1* gene, but
92 CpG dinucleotide methylation of its core promoter results in low *keap1* mRNA expression[42], making
93 them suitable for ectopically expressing kelch domain proteins with minimal interference from the
94 native KEAP1 protein. Sequence comparison clearly revealed that K13 is a homologue of KEAP1
95 (**Supplementary Fig. 1a**). We generated three stable transgenic lines expressing: (i) K13 as a C-
96 terminus fusion to GFP; K13-GFP, (ii) GFP alone, as well as (iii) a C-terminus fusion of flag-strep tag
97 KEAP1 (see *Materials and Methods*). Indirect immunofluorescence assays (IFA) with quantitative
98 analyses, suggested cellular distribution of K13-GFP, GFP and KEAP1, at comparable levels in
99 transgenic Du145 cells (**Supplementary Fig. 1b)**. K13-GFP, GFP and flag-strep tag KEAP1
100 respectively appeared as fusion proteins at expected sizes of 105-kDa, 27-kDa and 80-kDa
101 (**Supplementary Fig. 1c, d**).

102 We recently showed that *in vitro* heme bound recombinant K13 protein (TrK13-WT) with high
103 affinity[22], but action of heme in cells was not known. Since the K_d for heme binding to K13 protein was
104 61.5 nM, we wanted to measure the effects at low nanomolar concentrations of heme. This required
105 growing Du145 cells under conditions where available heme was substantially depleted from the
106 extracellular sources, and the production of biosynthetic heme was blocked by inhibitors. Fetal bovine
107 serum (FBS) is the largest extracellular donor of heme and contributed median concentration of 3.2 ±
108 0.06 μM heme to culture media. We reduced FBS concentrations of heme to <850 nM
109 (**Supplementary Fig. 2a, b**) to create heme-depleted media (HDM; *Material and Methods*). Since the
110 K_d of heme for albumins is >1 μM, this was expected to dramatically reduce the transfer of
111 extracellular heme to cells. We also added succinylacetone [SA; an inhibitor of the second enzyme of
112 heme biosynthesis pathway, δ-aminolevulinic acid (ALA) dehydratase] to the culture media, which
113 restricted intracellular *de novo* heme synthesis. Our overall goal was to achieve culture conditions that
114 would be responsive to nanomolar concentrations of exogenously added heme. Accordingly, under

115 HDM conditions, the parental Du145, transgenic GFP and K13-GFP cells all showed intracellular
116 concentrations of ~60 nM heme. Addition of extracellular heme at 5 μM, raised intracellular heme to
117 400-450 nM. When extracellular concentrations were raised to 50 μM, the intracellular levels
118 plateaued at ~750 nM (**Supplementary Fig. 2c**). Together these data suggested that in the course of
119 all experiments intracellular heme concentrations ranged from ~60-750 nM.

120 K13-GFP cells cultured in HDM (K13-GFP^{HDM}) were subsequently exposed to different concentrations
121 of exogenously added heme (0-5 μM) in the media (referred to as heme-replenished media). As
122 shown in **Fig. 1a**, concentrations of 10 nM heme induced detectable increase in K13-GFP levels.
123 Progressive increase of K13-GFP levels were seen at 50 nM, 100 nM, 1 μM and 5 μM heme. At 5 μM
124 heme, K13-GFP levels were restored to those seen in K13-GFP 'control' cultures (**Fig. 1b**). There was
125 no effect on the cellular viability of K13-GFP (or GFP) expressing cells at 5 μM heme;
126 (**Supplementary Fig. 2d:** the IC_{50} for heme was ~25-fold higher for all cells). Notably, there was no
127 detectable change in the relative intensity of GFP or KEAP1 proteins when cells were subjected to
128 heme depletion or when supplemented with 5 μM heme (**Supplementary Fig. 2e, f**).

129 We next investigated the specificity of heme action. As shown in **Fig. 1c,** PPIX alone or when
130 complexed with Zn, had no effect even at 50 μM. However, increasing heme levels from 5 to 50 μM
131 continued to steadily increase levels of K13-GFP. Together, the data suggest that heme at
132 extracellular concentrations of 10 nanomolar or higher (and up to 50 μM) increase cellular levels of
133 K13-GFP (but not GFP or KEAP1), suggesting it is specific for K13. Increases in K13 were only
134 mediated by heme (not PPIX or Zn-PPIX) and likely due to heme's directly binding to K13 (since we
135 have previously shown that heme binds K13 with nanomolar affinity *in vitro*[22]).

136 Amongst heme binding proteins, hemopexin, a serum glycoprotein (which displays highest affinity for
137 heme at K_d ~ 1 pM[43,44]) has been reported to show heme-dependent resistance to protease
138 digestion[43]. We therefore investigated if the protease sensitivity of K13 was altered in its heme-bound
139 state. For *in vitro* assay, we used the affinity purified 61-kDa recombinant TrK13-WT protein as K13
140 representative, described in our previous studies[22,45]. Recombinant TrK13-WT protein (10 μM) was
141 incubated with or without equimolar concentrations of heme and desalted to remove excess unbound
142 heme (see *Materials and methods*). Heme-bound TrK13-WT protein was subsequently treated with
143 trypsin under optimal buffer and pH conditions for varied incubation times. For trypsin (a serine

144 protease that cleaves between the carboxyl group of arginine or lysine and the amino group of the
145 adjacent amino acid), we also included commercially procured BSA, a confirmed heme-binding
146 protein[46] (but with substantially lower affinity) as a control. As shown in **Fig. 1d**, Coomassie-stained
147 SDS-PAGE revealed full-length (FL) TrK13-WT protein at 61-kDa. Treatment with trypsin yielded
148 additional low molecular weight fragments (doublets at 30-kDa and at 12-kDa; blue arrowheads) in
149 the absence of heme, whose appearance was blocked when the TrK13-WT protein was pre-
150 incubated with heme. Heme-binding only conferred partial resistance of BSA to trypsin
151 (**Supplementary Fig. 2g**). In absence of heme, multiple small protein fragments were detected (from
152 22-40 kDa; green arrowheads), while in its presence, larger fragments were observed at 45-55-kDa
153 (red arrowheads). The effects of heme on trypsin digestion of both TrK13-WT protein and BSA were
154 likely because of changes in the 3-dimensional conformation of these proteins (which is consistent
155 with previous reports in the literature[46] and observed in our earlier CD studies[22]). As shown in **Fig. 1e**,
156 resistance to trypsin digestion was not seen when the TrK13-WT protein was incubated with PPIX or
157 Zn-PPIX or iron salts (ferrous ammonium sulfate, FAS or ferric ammonium sulfate, FES, although
158 these salts are known to bind K13)[22]. Together, these data suggest that heme binding to K13 shows
159 chemical and molecular specificity, may induce confirmational change and thereby induce
160 stabilization of K13 in cells.

161 **Heme alters K13-regulated oxidative stress responses**

162 Nuclear factor erythroid 2-related factor 2 (Nrf2) is a major redox-regulated transcription factor
163 controlled by KEAP1[47], the closest mammalian orthologue of K13. We therefore assessed whether
164 Nrf2 was regulated by K13 and the impact of heme, a known, major redox regulator[48]. First, we
165 investigated changes in Nrf2 levels in GFP or KEAP1 expressing cells under HDM or heme-
166 replenished culture conditions *i.e.,* GFP^{HDM} *versus* GFP^{HEME} or $KEAP1^{HDM}$ *versus* $KEAP1^{HEME}$ cells.
167 Relative intensities of both GFP and KEAP1 proteins remained unaffected by heme (**Supplementary**
168 **Fig. 3a, b**). Consequently, we investigated only K13-GFP cells, cultured in the absence or presence
169 of increasing concentrations of heme, and followed by immunoprecipitations from cellular lysates
170 using anti-GFP antibodies. Western blot (**Fig. 2a**) and quantitative densitometric analysis (**Fig. 2b**) of
171 band intensities revealed increasing amounts of immunoprecipitated K13-GFP with increased heme
172 concentrations (**2a i** and **2b i**). In contrast, levels of co-immunopurified Nrf2 decreased with increasing

173 heme (**Fig. 2a i**), although there was increase in the overall cellular Nrf2 levels (**Fig. 2a ii** and **2b ii-**
174 **iii**). These results strongly implied that interactions between K13 and Nrf2 were negatively affected by
175 heme. To investigate whether these reflected direct protein-protein interactions, we co-incubated
176 recombinant Nrf2-6×his protein with either heme-free or heme-bound recombinant TrK13-WT (that
177 was desalted to remove excess unbound heme). As shown in **Fig. 2c**, after incubation with heme for
178 1 h, there was ~26% reduction in Nrf2-6×his binding to TrK13-WT, suggesting heme may directly
179 prevent/disrupt Nrf2 binding to K13.

180 We next performed immunolocalization studies to determine subcellular distribution of Nrf2 in K13-
181 GFP^{HDM} and K13-GFP^{HEME} cells (**Fig. 2d**). Here, data revealed predominantly cytoplasmic localization
182 of Nrf2 with K13-GFP under HDM conditions (left panel). In contrast, the K13-GFP^{HEME} cells displayed
183 prominent nuclear localized Nrf2 protein (right panel). Moreover, in the presence of heme, levels of
184 K13 were higher than under HDM conditions. Subcellular fractionation confirmed that under
185 conditions of HDM, a vast majority (~83%) of Nrf2 protein was detected in the cytoplasmic fraction
186 (**Fig. 2e**; second blot). However, in the K13-GFP^{HEME} cells, ~87% of the Nrf2 protein was detected in
187 the nuclear fraction. As expected, the K13-GFP protein was present exclusively in the cytoplasmic
188 fraction independent of the absence or presence of heme. Furthermore, the intensity of K13-GFP was
189 much higher under heme-replenished condition (top blot). The GFP expressing cells revealed no
190 changes in the relative nuclear/cytoplasmic fractionation of the Nrf2 protein or intensities of GFP
191 (**Supplementary Fig. 3c**). As Nrf2 is a redox-controlled transcription factor, we also compared the
192 expression of stress-response genes *heme oxygenase* (*ho-1*), *NAD(P)H quinone oxidoreductase 1*
193 (*nqo1*) and *thioredoxin reductase 1* (*txnrd1*) in K13-GFP^{HDM} and K13-GFP^{HEME} cells. As shown in **Fig.**
194 **2f**, RT-qPCR data confirmed increased expression of these stress-response genes as a consequence
195 of increased Nrf2 translocation to the cell nucleus.

196 **Chaperone mediate autophagy is a major pathway of K13 degradation.**

197 A recent study implicated chaperone-mediated autophagy (CMA) in the lysosomal degradation
198 KEAP1 in mouse midbrain progenitor cell line SN4741[49]. Since K13 shares structural and sequence
199 identity with KEAP1, we investigated if similar degradation pathway was involved in the proteolysis of
200 K13-GFP under HDM conditions. Our analyses of the primary sequence of K13, suggested it
201 contained 'KFERQ-like' motifs as recognized by an online algorithm KFERQ finder v0.8

202 (*https://rshine.einsteinmed.edu*)[50]. These motifs are targeting signals of CMA. In CMA the chaperone
203 heat shock 70-kDa (cognate) protein 8 (also known as HSPA8) binds 'substrate' proteins bearing
204 'KFERQ-like' motifs[51,52]. LAMP2A acts as a receptor on the lysosomal membrane. HSPA8 binds the
205 cytosolic tail of LAMP2A[53]. This in turn unfolds the substrate and enables its translocation into
206 lysosomes where it is subsequently degraded[54]. As shown in **Fig. 3a**, K13 contains eighteen 'KFERQ-
207 like' motif, strongly suggesting it may be targeted to lysosomes. Immunolocalization studies using
208 indirect IFA suggested moderate association between K13 and LAMP2A with Pearson's correlation
209 coefficient (PCC) of 0.59. Notably, heme raised the PCC to 0.79, suggesting it induced a high level of
210 co-association of K13-GFP with LAMP2A (**Fig. 3b**). We therefore concluded that although heme
211 induces conformational change in K13, this does not obscure targeting of K13-GFP to LAMP2A
212 labeled lysosomes. But since heme increases levels of K13, it is not likely to promote degradation of
213 K13-GFP within the lysosome. We therefore propose (as schematic in **Fig. 3b**) that the heme-induced
214 conformational stability may prevent unfolding of the K13-GFP substrate and its translocation into the
215 lysosome, thereby limiting its degradation in cells**.**

216 Since LAMP2A is an exclusive CMA marker, we investigated the effects of a previously reported
217 CMA-inhibitor, *i.e.*, the RARα (retinoic acid receptor alpha) activator ATRA (*all-trans* retinoic acid),
218 known to be a potent inhibitor of LAMP2A expression[55]. As expected, under HDM conditions, there
219 was moderate co-association of K13 and LAMP2A, with a PCC of 0.58 (**Fig. 4a i**). Treatment with
220 ATRA elevated levels of K13-GFP as well as its co-association with LAMP2A (raising the PCC to
221 0.90; **Fig. 4a ii**). As expected, heme also increased K13-GFP levels and the PCC with LAMP2A rose
222 to 0.77 (**Fig. 4a iii**). Notably, ATRA markedly increased K13-GFP in HDM to levels far higher than
223 those seen with heme replenishment (**Fig. 4b i** and **4b iii**). ATRA also significantly reduced LAMP2A
224 levels compared to controls, both in K13-GFP^{HDM} and K13-GFP^{HEME} cells (**Fig. 4b i** and **4b ii**).
225 Together these data strongly suggested ATRA-mediated reduction of LAMP2A prevented the
226 degradation of K13, explaining why it increased K13 levels more than heme.

227 To further confirm the role of LAMP2A-mediated degradation of K13-GFP, we obtained stable
228 transgenic cell lines expressing K13-GFP or GFP in the HeLa *lamp2a* knockout (*Δlamp2a*; Abcam;
229 ab255402) and the corresponding parental HeLa cells (Abcam, ab255928). HeLa cells have
230 previously been reported to inherently express very low levels of native KEAP1 protein and

231 correspondingly have high basal Nrf2 activity[56]. We designated them as *Δlamp2a*$^{K13\text{-}GFP}$, HeLa$^{K13\text{-}GFP}$,
232 *Δlamp2a*^{GFP} and HeLa^{GFP}, cells, respectively. As shown in **Supplementary Fig. 4a**, LAMP2A protein
233 was undetectable in *Δlamp2a* cells both by fluorescence microscopy and in western blots. Moreover,
234 there was no difference in levels of K13-GFP in the transgenic *Δlamp2a*$^{K13\text{-}GFP}$ cells regardless of
235 whether they were cultured under HDM or 5 μM heme-supplemented conditions (**Fig. 4c**). In contrast,
236 significant reduction in the K13-GFP level was evident in the parental HeLa$^{K13\text{-}GFP}$ cells in HDM
237 (compare lanes 3 and lane 4). In *Δlamp2a*^{GFP} cells, we observed no changes in the level of GFP
238 (**Supplementary Fig. 4b**) when compared to the HeLa^{GFP} cells irrespective of HDM or heme-
239 replenished conditions. Thus, the absence of LAMP2A adversely affected the proteolysis of K13-GFP,
240 but not GFP, which further substantiated the involvement of CMA pathway in proteolysis of K13-GFP
241 under HDM conditions.

242 **K13's kelch domain transfers heme-dependent stability and heme binding property to KEAP1**

243 We next investigated if the heme-regulated stability of K13 was due to its kelch repeat (KRP) domain
244 and could be transferred to KEAP1. As shown in **Fig. 5a**, we made chimeras of the N-terminus of
245 KEAP1 and the kelch domain of K13 fused to GFP (KEAP1^{N}K13^{KRP}-GFP) as well N-terminus of K13
246 and the kelch domain of KEAP1 fused to GFP (K13^{N}KEAP1^{KRP}-GFP). Stable expression of
247 KEAP1^{N}K13^{KRP}-GFP and K13^{N}KEAP1^{KRP}-GFP proteins in Du145 cells was confirmed by western
248 blots (**Fig. 5b**). As shown in **Fig. 5c**, immunolabeling assays revealed significant (72%) reduction in
249 KEAP1^{N}K13^{KRP}-GFP cells under HDM conditions when compared to respective counterparts in 5 μM
250 heme-supplemented media. In contrast K13^{N}KEAP1^{KRP}-GFP cells were reduced by only 30%.
251 Supplementing HDM with the heme precursor ALA had no significant effect, but heme largely restored
252 levels of KEAP1^{N}K13^{KRP}-GFP expression (**Fig. 5d)**. K13^{N}KEAP1^{KRP}-GFP showed much less heme-
253 responsive expression (**Fig. 5e**). Together, these results suggested that the kelch domain of K13
254 conferred robust heme-stimulated expression of the KEAP1-K13 chimera which was closely
255 comparable to the wild-type K13-GFP. The NTR, CCD and BTB-POZ domains of K13 also made a
256 minor contribution in transferring heme-dependent phenotype to the KEAP1 chimera.

257 In addition, we investigated the relative affinity of recombinant K13 (also known as TrK13-WT),
258 KEAP1, KEAP1^{N}K13^{KRP} and K13^{N}KEAP1^{KRP} proteins for hemin-agarose. Recombinant proteins

259 expressed and purified from *E. coli* were incubated with hemin-agarose beads and percentage
260 binding was determined (see *Materials and Methods*). As shown in **Fig. 5f**, K13/TrK13-WT, KEAP1,
261 KEAP1^{N}K13^{KRP} K13^{N}KEAP1^{KRP} proteins respectively showed 30.1%, 5.9%, 32.5% and 10.3% binding
262 to hemin-agarose, respectively. Again, this suggested that the kelch domain of K13 could confer the
263 same efficiency of heme binding to KEAP1 as seen associated with K13/TrK13-WT protein. When
264 soluble cellular extracts from stable transgenic Du145 cells ectopically expressing the K13-GFP,
265 KEAP1 and their chimera proteins were used, we again found that K13-GFP, KEAP1,
266 KEAP1^{N}K13^{KRP}-GFP and K13^{N}KEAP1^{KRP}-GFP bound hemin-agarose beads with efficiencies of
267 58.9%, 3.1%, 64.5% and 29.3%, respectively (**Fig. 5g**). Cumulatively, the results in **Fig. 5** strongly
268 support that the kelch domain of K13 transfers robust heme binding capacity and heme-based
269 stabilization to KEAP1. The N-terminal domains of K13 may also contribute a minor role consistent
270 with our prior studies suggesting a subset of heme binding motifs are also detected outside of K13's
271 Kelch domain[22].

272 **K13 and its chimeras confer sensitivity to heme-dependent ART-killing of Du145 cells**

273 Since heme is implicated in the activation of ART, we next assessed the ART sensitivity of Du145
274 cells expressing K13-GFP and its chimeras (as well as GFP alone) in a standard killing MTT [3-(4,5-
275 dimethylthiazol-2-yl)-2,5-diphenyltetrazolium bromide] assay (see *Materials and Methods*) comparing
276 outcomes in HDM or media replenished with 5 μM heme. Du145 cells expressing control GFP
277 showed an IC_{50} of 117.7 ± 0.9 μM in the absence of added heme (**Fig. 6a i**), thereby indicating that
278 they are intrinsically highly resistant to ART. The addition of 5 μM heme minimally reduced the IC_{50} by
279 2.6%. Expression of KEAP1 also showed a small effect inducing approximately 6.1% reduction.
280 However, K13-GFP and the KEAP1^{N}K13^{KRP} cells had a greater effect, which translated into increasing
281 heme-dependent sensitivity to ART by 18.2% and 23.7%, respectively (**Fig. 6a i-ii**). K13^{N}KEAP1^{KRP}-
282 GFP had lesser effect showing ART sensitivity increase of 13.5%. The relative order of conferring
283 increased ART sensitivity was KEAP1^{N}K13^{KRP}-GFP > K13-GFP > K13^{N}KEAP1^{KRP}-GFP > KEAP1 >
284 GFP, which matched the heme binding properties reported for these transgenes in **Fig. 5**. Together,
285 these data suggested that the presence of K13, particularly its kelch domain, conferred sensitivity to
286 ART in the presence of 5 μM heme.

287 Since the K13 also binds Nrf2 (which is antagonized by heme), we examined the effects of ART on
288 the dynamics of K13 and Nrf2 in HDM as well as after heme supplementation. As shown in **Fig. 6b i-**
289 **ii,** ART had no sizeable effect on K13-GFP levels in the presence or absence of heme. However, Nrf2
290 levels were reduced by 50% in the presence of both ART and heme. This reduction was due to the
291 depletion of Nrf2 in the cytoplasm (**Fig. 6c i-ii**), suggesting it was through regulation by K13. These
292 data support a model shown in **Fig. 6d**, where heme plays a major role in binding K13 to displace
293 Nrf2, which in turn is targeted to the nucleus to induce a protective redox (or pro-survival) response.
294 Heme bound to K13 activates ART to generate toxic heme-ART adducts. K13's renewed ability to
295 regulate Nrf2 suggests that these toxic heme-ART adducts do not inactivate K13. Rather, the adducts
296 dislodge from K13 and disperse to mediate damage which occurs in absence of a protective redox
297 response, resulting in cell death (or pro-death) responses. Thus, ART-induced killing reconstituted in
298 Du145 cells may arise from the dual effect of inducing toxic ART-heme adducts as well as preventing
299 a protective redox response to render an overall 'pro-death response (**Fig. 6d**).

300 **ART sensitivity is increased proportional to the K13 intensity**

301 Our findings in **Fig. 6** strongly supported that expression of K13 or chimeras, containing its kelch
302 domain in presence of 5 μM heme, increased sensitivity to ART. We wanted to gain better
303 understanding on whether increasing K13 at sub-micromolar heme concentration also played a role.
304 Since our studies in **Fig. 4** established that ATRA increased levels of K13, we separately evaluated
305 the effects of heme and ATRA. As shown in **Fig. 7a, b**, in cells expressing GFP, 5 μM heme
306 increased sensitivity to ART by ~ 6%, while ATRA had no effect. In K13-GFP cells, heme alone
307 stimulated ART-sensitivity by 18%, ATRA by 25%, and the combination of two stimulated ART-
308 sensitivity by 36% (**Fig. 7a, b**). These data strongly suggested that elevation in levels of K13-GFP by
309 ATRA even under HDM conditions increased sensitivity to ART. But heme at 5 μM provided additional
310 sensitization effect possibly by (i) increasing K13 levels (ii) providing substrate to form toxic heme-
311 ART adducts, whose disassociation from K13 suppression of pro-survival responses (as hypothesized
312 in **Fig. 6d**).

313 We were therefore interested in determining whether ART sensitivity was proportional to K13
314 intensity. To do so, we compared the sensitivity to killing by ART to levels of K13 (or its kelch chimera)
315 normalized to GAPDH (a control cytoplasmic protein). As shown in **Fig. 7c**, we observed an overall

316 linear relationship between increase in ART sensitivity and the K13/GAPDH (R^2 value = 0.97).
317 Notably, cell lines designated as 1, 2 and 4 reflected measurements generated in HDM, and all
318 showed lower degree of ART sensitivity and K13/GAPDH levels than counterpart measurements
319 generated in the presence of 5 μM heme. Also, the presence of ATRA increased K13 levels, thereby
320 boosting K13/GAPDH ratio and correspondingly showed increased ART sensitivity of K13-GFP cells
321 under HDM conditions (as cell line #3 in **Fig. 7c**). Moreover, combination of heme and ATRA in these
322 cells (designated as 3H) further elevated K13/GAPDH ratio and showed highest sensitivity to ART
323 (38%). Comparisons in HeLa cells revealed that knockout of LAMP2A, which increased K13/GAPDH
324 by three-fold raised ART sensitivity by one-third. However, 5 μM heme further raised the K13/GAPDH
325 ratio four-fold and doubled ART-sensitivity (compared to parental HeLa in HDM).

326 When we separately compared the effects of extracellular 5 μM *versus* 50 μM heme (**Fig. 7d**), the
327 higher concentration of heme further augmented killing. In GFP cells, this could be easily interpretable
328 as increasing intracellular heme alone from ~400 to 750 nM directly sensitized ART-killing, increasing
329 it from ~2 to ~6%. However, as we have previously shown for K13 kelch domain proteins, heme may
330 also act by raising levels of the transgene alone. We therefore tracked transgene expression at 50 μM
331 heme (**Fig. 7d**, black bars). This revealed that even at 50 μM, increasing K13-GFP and K13 chimeras
332 stimulated ART-killing to much higher levels. Taken together, these data suggest that heme alone (at
333 intracellular concentrations of 400 nM to 1 μM), is comparatively weak stimulator of ART's killing
334 activity but can be potentiated by expression of K13 and its appropriate chimeras.

335 **Discussion**

336 The Du145 cell model enabled assessment of the effects of K13 binding to heme in the nanomolar to
337 micromolar range. The intrinsic concentration of heme in Du145 cells is 60 nM. Supplementing with
338 extracellular heme at 5 μM, resulted in maximal intracellular concentrations of 0.45 μM which is lower
339 than the physiological range (1-5 μM) reported for *Plasmodium*[38,39]. Although kelch proteins bind a
340 wide range of protein-partners[20,57–59], this is first report that a small molecule like heme can bind a
341 member of this evolutionary conserved family. Whether kelch proteins of other apicomplexans bind
342 heme is not known. Remarkably, the kelch domain of K13 is necessary and sufficient to confer heme
343 binding to its closest mammalian orthologue KEAP1. Whether and how heme is released from K13
344 under physiological conditions is not known. Heme, as a small molecule bound to K13 cannot be

345 ubiquitinylated and degraded, which is a hallmark of protein substrates and their cellular regulation by
346 kelch proteins. But our studies suggest that when K13-bound heme activates ART, the kelch structure
347 may protect against self-oxidation by heme-ART adducts. This is consistent with prior studies showing
348 that alkyne-ART analog despite being highly active against a wide range of malarial cellular targets
349 failed to alkylate K13[60,61]. Moreover, the heme-ART adducts are known to show low affinity for
350 recombinant K13[22], suggesting a mechanism for their release and a new model where a single
351 molecule of K13 may catalyze multiple cycles of ART-heme activation (**Fig. 8a**; K13 cycle 1). Since
352 heme is known to be a strong oxidant[29], it is highly likely that upon its binding to K13, a protective
353 redox response will be elicited as a compensatory response (that is expected for cycles 2 and 3
354 shown in **Fig. 8a**) but whether *Plasmodium* encodes for functional orthologue of Nrf2 (the transcription
355 factor that induces the stress-induced protective response in Du145 cells) remains unknown.

356 The model in **Fig. 8a** is informative for ring as well as trophozoite stage death of malaria parasites. As
357 in the Du145 model, for both parasite stages we propose a pro-death response induced by addition of
358 ART to K13-heme, which releases activated and toxic ART-heme adducts. In rings, heme is likely to
359 be derived from parasite mitochondrial sources as well as host *milieu*, while trophozoite stages may
360 have an additional source, namely hemoglobin-derived heme (although most of this is converted to
361 hemozoin). That intracellular heme concentrations of 400- 750 nM alone showed low sensitization to
362 ART counters prevailing models that suggest that heme alone is sufficient to activate ART at the
363 trophozoite stages (**Fig. 8b**). Yet we found that even at the lowest intensities, K13 (expected not to
364 exceed nanomolar levels) was more effective than heme alone and in addition, the extent of
365 sensitization was directly proportional to the level of K13. This is consistent with our findings that
366 raising K13 (by ATRA treatment) in HDM (with 60 nM heme), increased ART-sensitivity more than an
367 eight-fold elevation in free heme concentrations (to 400 nM). This strongly supports the idea that K13
368 acts as 'catalyst' to facilitate assembly of ART-heme complexes, and once the activated toxic adducts
369 are released, K13 may facilitate successive rounds of ART-based killing. We therefore propose that
370 rather than heme alone at the trophozoite, heme and K13 act together to effect sensitization to ART
371 (**Fig. 8c**). These stages are known to be more sensitive than rings, which is consistent with their
372 higher levels of both K13 and heme.

373 Our finding of K13 localization to late endosomes in Du145 cells is noteworthy because K13 has been
374 found on *P. falciparum* vesicles and endosomes and is best characterized in the FV of *P. falciparum*
375 trophozoites. These stages also express increased levels of K13 which concentrate on the
376 cytoplasmic face of electron dense 'cytostomes'[62] at the FV. Genetic depletion of K13 disrupts the
377 cytostome structure as well as endocytic uptake of hemoglobin[21]. Apicomplexan endosomes are
378 broadly classified as 'micropores and the malarial FV develops from a Type II micropore. All
379 apicomplexans (including *Plasmodium*) contain a 'Type I' micropore seen on 'apical' stages. Recently,
380 the *T. gondii* K13 orthologue was localized to Type I micropores and shown to regulate plasma
381 membrane endocytosis[63]. Plasmodial K13 is expressed in merozoite and ring stages, but whether it
382 localizes on parasite's Type I micropores is not yet established. By virtue of evolutionary conservation
383 of mechanisms of apical organelles, we have proposed that K13 localizes to *P. falciparum* Type I
384 micropores[64]. Endosomal location in Type I and Type II micropores of rings and trophozoites,
385 respectively may enable concentration of K13-heme, possibly to stabilize these structures which then
386 also create cellular foci to efficiently activate ART at all stages of intracellular parasite development.

387 That heme binding, endosomal concentration and ART-based killing are not properties of mammalian
388 KEAP1, suggests they are parasite evolutionary adaptations conferred by the K13 kelch domain. Yet,
389 orthologues of LAMP2A (a receptor for K13 in Du145 and HeLa cells that controls its autophagic
390 degradation), have not been reported in *P. falciparum* or *T. gondii.* Nonetheless, autophagic systems
391 exist in both parasites[65,66] and additional studies are needed to determine their influence on heme-
392 dependent K13 stability, as well as endosomal degradation turnover of K13 and its orthologues
393 across apicomplexans. Another key priority is identification of K13- coupled parasite redox factors that
394 remain unidentified because a lack of conservation at the level of primary sequences prevents easy
395 prediction from nucleotide sequence comparisons. While our studies establish that K13 is an
396 important determinant in ART sensitization, other oxidative factors may also contribute. Our present
397 study suggest Du145 may continue to provide a powerful model system for future functional screens
398 for endosomal effectors as well as novel parasite pro-oxidant responses, regulated by both heme and
399 K13 and targeted in killing by ART. The lessons learned may also reveal mechanisms to sensitize a
400 wider range of infectious agents as well as chronic disorders (like cancer) to killing by ARTs.

401 **Materials and methods**

402 **Generation of plasmid constructs**

403 The pPR-IBA101 (TrK13-WT) plasmid was generated as described in earlier studies[22,45]. For the
404 generation of pPR-IBA101 (KEAP1), the full length (1875 base pairs) transcript of *keap1* was
405 amplified from cDNA library prepared from human cell line (HEK293T) using the primer pairs (Hs-
406 Keap1-BsaI-Fwd (5'-CAAATGGGAGACCTTATGCAGCCAGATCCCAGGC-3') and Hs-Keap1-BsaI-
407 Rev (5'-CCAAGCGCTGAGACCAGCAGCACAGGTACAGTTCTGCTGGTCAATCTG-3'). The PCR
408 product was digested with BsaI and cloned at corresponding sites in similarly-digested pPR-IBA101.
409 For the generation of pPR-IBA101 ($KEAP1^{N}K13^{KRP}$), nucleotide sequences coding for the N-terminus
410 region of KEAP1 was amplified from pPR-IBA101 (KEAP1) plasmid using (Hs-Keap1-BsaI-Fwd and
411 KEAP1toK13-KRP-Rev (5'-AAATCCACCGGCAGCAGCGCGGCCCACCTTGGG-3') primers.
412 Nucleotide sequence encoding for the KRP region of K13 was amplified using the pPR-IBA101
413 (TrK13-WT) plasmid as template and KEAP1toK13-KRP-Fwd (5'-
414 GTGGGCCGCGCTGCTGCCGGTGGATTTGATGGTGTAGAATATTTAAATTCG-3') and PfKelch13-
415 BsaI-Rev (5'-GGAGGACAAAATGGCAATGTTCTAAATTCATGTGGATTCTTTTCACCAGAT
416 ACAAATGAATGGC-3') primer pairs. The two PCR products were used as templates to reconstitute
417 $KEAP1^{N}K13^{KRP}$ by overlapping PCR, which was then digested with BsaI and cloned into pPR-IBA101.
418 Similarly, to generate pPR-IBA101 ($K13^{N}KEAP1^{KRP}$), nucleotide sequences encoding for the N-
419 terminus of K13 was amplified from pPR-IBA101 (TrK13-WT) plasmid as template and PfKelch13-
420 BsaI-Fwd (5'-
421 CAAATGGGAGACCTTATGGAAGGAGAAAAAGTAAAAACAAAAGCAAATAGTATCTCG-3') and
422 K13toKEAP1-KRP-Rev (5'-GTAGATCAG
423 GGCAGCAGCTATACAAAATACTAATGGGAATGGTAAAAATTTAATACC-3') primers. Overlapping
424 PCR, using the above two PCR products as templates, generated $K13^{N}KEAP1^{KRP}$ which then
425 introduced to pPR-IBA101 after digestion with BsaI.
426 For generating recombinant Nrf2-6×his, the full length (1626 bp) transcript was amplified from cDNA
427 library prepared from human cell line (Du145) using the primer pairs HsNrf2-XbaIFwd (5'-
428 CACGTGTCTAGAATGATGGACTTGGAGCTGCCG-3') and HsNrf2ns-XhoIRev (5'-
429 CCTAGGCTCGAGGTTTTTCTTAACATCTGGCTTCTTACTTTTGGG-3') and the PCR product was
430 then digested with XbaI-XhoI and clone into similarly digested pET303-ct-his plasmid (ThermoFisher,
431 USA) for in-frame fusion with C-terminus 6×his tag. To generate GFP expressing constructs for

432 mammalian cells, pAcGFP1-C1 (Addgene, USA) was used and AgeI and NheI sites considered for
433 inserting the gene of interest. To generate pAcGFP1-C1 (K13-GFP), pAcGFP1-C1 (KEAP1^{N}K13^{KRP})
434 and pAcGFP1-C1 (K13^{N}KEAP1^{KRP}) plasmids, their pPR-IBA101 plasmids were used as
435 corresponding templates. For K13-GFP, the primers pairs were PfKelch13-NheI-Fwd (5'-
436 AAGCTTGCTAGCATGAACAGCGAGGTGTGTTCGCG-3') and PfKelch13-AgeI-Rev (5'-
437 AGCGCTACCGGTAGCAGCCAAATTTGCCAAGAGAATGCCGTG-3'), for generating
438 KEAP1^{N}K13^{KRP}GFP, the primer pairs were KEAP1-NheI-Fwd (5'-
439 AGATCTGCTAGCATGCAGCCAGATCCCAGGC-3') and PfKelch13-AgeI-Rev (5'-
440 AGCGCTACCGGTAGCAGCCAAATTTGCCAAGAGAATGCCGTG-3'); and for generating
441 K13^{N}KEAP1^{KRP}, PfKelch13-NheI-Fwd (5'-AAGCTTGCTAGCATGAACAGCGAGGTGTGTTCGCG-3')
442 and KEAP1-AAA-AgeIRev (5'-GGATCCACCGGTAGCTGCTGCACAGGTACAGTTCTGC
443 TGGTCAATC-3') primers were used. To generate the KEAP1 construct, pPR-IBA101 (KEAP1)
444 plasmid was used as the template to amplify nucleotides encoding for KEAP1-strep using KEAP1-
445 NheI-Fwd and Strep-XhoI-Rev (5'-GGATCCCTCGAGCTTTCTCGAACTGCGGGTGGCTCCAA-3').
446 The PCR amplified product was subjected to NheI-XhoI digestion and inserted into similarly digested
447 pAcGFP1-C1.
448 All constructs generated for this study were confirmed by Sanger's sequencing prior to further
449 experiments.

450 **Cell culture, generation of transgenic lines and their treatments**

451 The Du145 cell line was the kind gift from Prof. Rana Pratap Singh, SLS, JNU, India. The parental
452 HeLa (ab255928) and HeLa-Δ*lamp2a* (ab255402) were procured from Abcam, USA and cultured
453 according to the manufacturer's instructions in complete media RPMI (Gibco, USA). Cells were
454 transfected using Lipofectamine 3000 (Invitrogen, USA) following the manufacturer protocol. Stable
455 transgenic lines were generated by G418 (0.5 mg/ml, Sigma, USA) selection. For the heme depleted
456 (HDM) conditions, the cells were grown in RPMI media supplemented with heme-depleted FBS and
457 succinyl acetone (0.5 mM, Caymanchem, USA) for 48 h. For heme-replenished media 5 μM hemin
458 chloride (Merck, USA) was added to the HDM. To assess *in vivo* stability of K13 protein upon heme
459 binding, the cells were treated with heme analogs PPIX (50 μM, Merck, USA) or Zn-PPIX (50 μM,
460 Merck, USA) for 48 h. Cells were also subjected to treatment either with for 48 h with ART (50 μM,
461 Caymanchem, USA) in presence or absence of heme.

462 **Preparation of the heme-depleted FBS**

463 Commercially-purchased FBS (Gibco, USA) was incubated with ascorbic acid (10 mM, SRL, India) at
464 37°C in a shaking incubator at 200 rpm for overnight. Spectral scans of the pre- and post-treated FBS
465 measured to check the presence or absence of soret peak at 410 nm, respectively using JASCO
466 UV660 spectrophotometer. Finally, the ascorbate-treated FBS was dialyzed against PBS, pH 7.4, with
467 at least three periodic changes for 24 h at 4°C. Dialyzed FBS was filter-sterilized using 0.2 µm
468 polyether sulfone filter (Sartorius, USA).

469 **Assessment of cellular viability**

470 Cell viability was assessed using 3-(4,5-dimethylthiazol-2-yl)-2,5-diphenyltetrazolium bromide (MTT,
471 Merck, USA)-based colorimetric assay. Cells at 50-60% confluency and within 72 h incubation in the
472 96-well cell culture plate were only considered. Following treatment, the cells incubated with 20 µl of 5
473 mg/ml MTT solution for 2h at 37° in the dark. Finally, the culture media was discarded and formazan
474 crystal was dissolved with 200 µl of DMSO, and absorbance was recorded at 570 nm using a
475 microplate reader (Thermo Fisher Scientific, USA). Cell viability was calculated and expressed as
476 percentage in comparison to the untreated controls. For MTT assay, the viability was calculated for
477 six different concentrations (0, 40, 80, 120, 160 and 200 µM) in three replicates to generate the IC_{50}
478 values for ART.

479 **Estimation of total cellular heme content**

480 Cells were grown up to 90-95% confluency and dislodged from the plate by treating with trypsin and
481 were washed twice with saline PBS. Cell count was recorded prior to lysis using hemocytometer.
482 Cells were then solubilized in five volumes of RIPA buffer for 2 h at 4ºC. After a brief centrifugation,
483 the supernatant was diluted ten times and subjected for spectrophotometric scanning at 410 nm. The
484 absorbance was plotted against the standard curve of hemin chloride to calculate the total cellular
485 heme content. The standard curve has been generated using gradually increasing concentration (0,
486 0.05, 0.1, 0.5, 1 and 10 µM) of hemin chloride.

487 **Nuclear and cytoplasmic fractionation of transgenic cells**

488 Cellular fractionation into nuclear and cytoplasmic fractions was performed following previously
489 described protocol[67]. Briefly, the cells from the 60 mm culture plates were scrapped and washed twice

490 with ice-cold phosphate buffered saline (PBS) pH 7.4. The cell pellets were washed, resuspended in
491 250 µl of ice-cold 0.2% (v/v) NP40 (HiMedia Labs, India), minced with micro-pestle, vortexed and kept
492 on rocker shaker for 15 mins. The resuspended pellets were then centrifuged at 10,000 rpm for 1 min
493 and the supernatant was collected as the cytoplasmic fraction. The pellet was then resuspended in 1
494 ml ice-cold 0.2% (v/v) NP40 to remove remnant cytoplasmic debris and centrifuged at same speed.
495 Finally, the pellet was resuspended in 200 µl ice-cold PBS and designated as the nuclear fraction.
496 The nuclear fraction was also briefly sonicated using micro pulser (Sonics, USA).

497 **Indirect immunofluorescence assay (IFA)**

498 IFA was performed using the parental or transfected cell lines. Briefly, cells were initially grown on
499 poly-L-lysine coated coverslips and fixed using 4% (w/v) paraformaldehyde/ 0.0075% (v/v)
500 glutaraldehyde followed by permeabilization with 0.1% (v/v) Triton X-100 and neutralized with 50 mM
501 NH_4Cl. Blocking was done using 3% (w/v) BSA. The coverslips were incubated with respective
502 primary antibodies (10 µg/ml) at 4°C for overnight followed by incubation in FITC- or TRITC/
503 Rhodamine-conjugated secondary IgG antibodies (1:200; MP biomedicals, USA). Cellular nuclei were
504 stained with 5 µg/ml Hoechst 33342 (Molecular Probes) and slides were mounted with DABCO. The
505 slides were finally visualized by SP8 confocal laser scanning microscope (Leica, Germany).
506 Fluorescence intensity was calculated using Image-J software (*https://imagej.net/ij/*) software by
507 considering 3 biological replicates for each set and each replicate containing 30 individual cells. The
508 RGB intensity plot and Person's correlation coefficient (PCC) was generated from the Image-J
509 graphics and JaCop, respectively.

510 **SDS-PAGE and western blotting**

511 The induced bacterial cell pellet was directly solubilized in Laemmli's sample buffer and heat
512 denatured for 15 min at 95ºC. For mammalian cells, following scrapping from plates, cells were
513 washed twice with saline PBS and solubilized in five volumes of RIPA buffer for 2 h at 4ºC. After a
514 brief centrifugation, the supernatant was considered as whole protein pool and boiled for 15 min at
515 95ºC using Laemmli's sample buffer and resolved by 8-10% SDS-PAGE followed by Coomassie or
516 silver staining. For subsequent western blots, resolved proteins were transferred into nitrocellulose
517 membrane (MDI, USA) followed by blocking with ice cold 5% (w/v) fat-free skim milk (SRL, India) for 2
518 h at RT. The membranes were incubated with specific primary antibodies (1:3000 to 1:5000 dilution)

519 for overnight at 4ºC on a platform shaker followed by subsequent washing and incubation with
520 respective HRP-conjugated secondary antibodies (1:7000 to 1:10000 dilution). Blots were finally
521 developed by ECL assay and detected using gel imager (Bio-Rad, USA). The primary antibodies are
522 used in this study were: anti-GFP (Invitrogen, USA; Cloud clone, China), anti-UBQ, anti-Lamp2 and
523 anti-GAPDH (Cloud clone, China), anti-k13 (Custom generated, Biobharati Life Sciences[45]), anti-
524 Histone 3 (kind gift from Prof. Suman Kumar Dhar, SCMM, JNU, India), anti-Nrf2, anti-KEAP1, anti-
525 HO1, anti-NQO1, anti-MCM3, anti-DPP3 and anti-TRAF2 (ABclonal, Woburn), anti-His and
526 streptavidin-HRP (BioBharati Life Sciences, India), and anti-HA. The subsequent HRP conjugated
527 secondary antibodies used in this study were goat anti-rabbit (Bio-Rad, USA), goat anti-mouse, goat
528 anti-rat (MP biomedicals, USA). Band intensity was calculated from Image-J (*https://imagej.net/ij/*)
529 software by considering 3 individual blots for each data set.

530 **Purification of recombinant protein and *in vitro* trypsin digestion**

531 Recombinant Trk13-WT, KEAP1, $K13^{N}KEAP1^{KRP}$and $KEAP1^{N}K13^{KRP}$ proteins as C-terminus fusion
532 with strep tag and Nrf2-6×his were purified from isopropyl-1-thio-β-D-galactopyranoside (IPTG, SRL,
533 India) and arabinose (0.2%, SRL, India) induced bacterial pellet. Briefly, the induced bacterial pellet
534 was lysed using lysozyme (SRL, India), sonicated and washed thrice with 2% (w/v) sodium
535 deoxycholate (SRL, India) to purify inclusion bodies (IBs). The IBs was dissolved into 2 M urea, 50
536 mM Tris-HCl buffer pH 12.5 and then dialyzed against buffer W (50 mM Tris-HCl, 150 mM NaCl, pH
537 8). Dialyzed solution was kept for binding to StrepTactin XT Superflow resin (IBA, Germany) for
538 Trk13-WT, KEAP1, $K13^{N}KEAP1^{KRP}$and $KEAP1^{N}K13^{KRP}$ and Ni-NTA resin (Thermo, USA) for Nrf2-
539 6×his. Purified proteins were dialyzed overnight at 4°C against buffer W with at least three periodic
540 changes. Purity of each protein was checked by SDS-PAGE and Coomassie staining and further
541 confirmed by western blotting using commercial antibodies against the 6×his tag, strep tag (Biobharati
542 Life Sciences) or custom-generated anti-K13.

543 For *in vitro* trypsin digestion, 10 µg of recombinant TrK13-WT or commercially procured BSA (A3294,
544 Sigma, USA) was incubated with or without equimolar concentrations of heme in buffer W for 1 h.
545 Samples were desalted as described in our earlier study[22], and treated with 0.5 µg trypsin (T6567,
546 Sigma-Aldrich) for different incubation times. Following digestions, Laemmli's sample buffer was

547 immediately added to each sample, boiled for 15 min at 95˚C and processed for SDS-PAGE and
548 Coomassie staining.

549 ***In vitro* protein-protein interactions**

550 The purified recombinant Nrf2-6×his (10 μM) was incubated with Ni-NTA beads for overnight and
551 washed thrice with buffer W containing 30 mM imidazole. The Ni-NTA bound recombinant Nrf2-6×his
552 was then incubated with purified recombinant TrK13-WT (10 μM) in buffer W for 4 h at RT. The beads
553 were thoroughly washed with buffer W, and Ni-NTA-bound proteins were resolved by SDS-PAGE
554 followed by Coomassie staining or western blot using antibodies against the 6×his tag, strep-tag
555 (Biobharati Life Sciences) or custom-generated anti-K13. For experiments involving the interactions
556 between heme-bound or heme-free recombinant TrK13-WT and Nrf2-6×his, the TrK13-WT was
557 preincubated with heme (0 or 10 μM) at RT for 1 h at room temperature (RT) and desalted using PD
558 Spintrap™ G-25 columns (Cytiva) to remove excess unbound heme.

559 **Hemin agarose binding**

560 Affinity-purified recombinant Trk13-WT, KEAP1, $K13^{N}KEAP1^{KRP}$and $KEAP1^{N}K13^{KRP}$ proteins (10 μM)
561 were incubated with 50 μl suspensions of 50% v/v hemin-agarose (Merck, USA) beads for 1 h at RT
562 in buffer W, pH 8, under rotating conditions, followed by five washes with ten volumes of buffer W to
563 remove unbound proteins. The hemin-agarose beads were then solubilized in Laemmli's sample
564 buffer, resolved by SDS-PAGE, and visualized by Coomassie staining. For assessing hemin-agarose
565 binding from transgenic cellular lysates, the total cell pellet was resuspended in 5 volumes of ice-cold
566 RIPA buffer complemented with 1X protease inhibitor cocktail (cOmplete, Roche) and incubated at
567 rotating wheel for 1 h. After centrifugation (15 mins, 21,100 × g, 4ºC), the supernatant containing
568 soluble proteins fractions was incubated with hemin agarose beads for 4 h. Unbound proteins in the
569 lysates were washed with ten volumes of RIPA buffer and bound fractions were then solubilized in
570 Laemmli's sample buffer and subjected to western blotting using anti-strep tag antibody (Biobharati
571 Life Sciences).

572 **Co-immunoprecipitation**

573 Protein A beads (IBA Life Sciences, Germany) were incubated with 10 μg of respective primary
574 antibodies for 4 h at 4 ˚C under rotating conditions and unbound antibodies were removed by

575 extensive washes with pre-cooled PBS. Mammalian cells were harvested, lysed with five volumes of
576 RIPA buffer supplemented with 1 mM PMSF (Thermo, USA) and protease inhibitor cocktail (Roche)
577 and centrifuged at 10,000 × g for 15 min at 4ºC to remove the cell debris. Clarified lysates were then
578 incubated with antibody-coated protein A beads (30-50 µl, 50% v/v resuspension) for overnight at 4ºC
579 under rotating conditions. Following binding, unbound lysates were removed and the beads washed
580 twice with RIPA buffer and twice with ice-cold saline PBS. Beads were boiled with Laemmli's sample
581 buffer for 15 min at 95˚C and processed for western blotting.

582 **Total RNA, cDNA synthesis, and real time RT qPCR**

583 The total RNA was isolated by Trizol reagent (Invitrogen, USA). Briefly, cell pellets was washed twice
584 with PBS and homogenized using 500 µl of Trizol reagent. The supernatants were isolated after a
585 brief centrifugation, mixed with 300 µl chloroform and incubated at RT. After centrifugation at 13,000 ×
586 g for 15 min at 4ºC, the upper aqueous phase was removed and 500 µl isopropanol added. Following
587 incubation for 30 min at RT, the tubes were centrifuged at 13,000 × g for 15 min at 4ºC. The pellet
588 was washed twice with 70% ethanol and finally dissolved in TE. Samples were treated with DNase I
589 enzyme (Thermo scientific, USA) to remove genomic DNA contamination. The quantity and quality of
590 RNA was estimated using Bio spectrophotometer (Eppendorf, Germany) and agarose-formamide gel
591 electrophoresis. Approximately 1 µg of total RNA was used for cDNA synthesis using PrimeScript 1st
592 strand cDNA Synthesis Kit (Takara-Bio, Japan) following manufacturer's protocol. For real time RT-
593 qPCR analyses, 2 µl of ten-fold diluted stock solution of cDNA samples was used. To perform RT-
594 qPCR analyses, primers were designed based on the coding sequence of specific genes using Oligo
595 Analyzer software (*https://eurofinsgenomics.eu/en/ecom/tools/oligo-analysis/*). Primers pairs were
596 HsHO1_RT_Fwd (5'-ATGACACCAAGGACCAGAGC-3') and HsHO1_RT_Rev (5'-
597 GCATAAAGCCCTACAGCAACT-3'); HsNQO1_RT_Fwd (5'-CCTTCCGGAGTAAGAAGGCAG-3') and
598 HsNQO1_RT_Rev (5'-TCCAGGCGTTTCTTCCATCC-3'); HsTXNRD1_RT_Fwd (5'-
599 GGAACTAGATGGGGTCTCGG-3') and HsTXNRD1_RT_Rev (5'-TCTTGCAGGGCTTGTCCTAA-
600 3'). RT-qPCR analyses were performed by using HOTFIRE Pol EvaGreen qPCR Mix Plus (ROX)
601 (Solis BioDyne, USA) and Step one plus system (Applied biosystem, USA). To confirm the absence of
602 any primer dimers in the amplified products, a standard melting curve analysis was conducted.
603 Primers for *gapdh* included HsGAPDH_RT_Fwd (5'-CAGGAGGCATTGCTGATGAT-3') and

604 HsGAPDH_RT_Rev (5'-GAAGGCTGGGGCTCATTT-3') as reference. Relative fold change was
605 calculated by $2^{-\Delta\Delta Ct}$ method.

606 **Statistical validation**

607 One-way ANOVA was carried out to test significance in difference considering at least three biological
608 replicates using GraphPad prism 10. The adjusted p values (p.adj ≤ 0.001) were obtained via Tukey's
609 HSD.

610 **Author contributions**

611 Conceptualization Ideas: S.D., K.H., S.B.[1] and S.B.[2].
612 Methodology: S.D., M.F.
613 Validation: S.D.
614 Investigation: S.D.
615 Resources: S.B.[1], S.B.[2], K.H.
616 Writing: S.D., K.H., S.B.[1]
617 Supervision: K.H., S.B.[1]
618 Project Administration: S.B.[1]
619 Funding acquisition: S.B.[1]
620

621 **Acknowledgements**

622 This work was supported by research grants from the Indian Council of Medical Research (ICMR),
623 (58/25/2020/PHA/BMS) and Indian Ministry of Human Resource Development (MHRD) Scheme for
624 Translational and Advanced Research in Sciences (STARS) (MoE-STARS/STARS-2/2023-0111) from
625 the Government of India (SB). SD is a recipient of Department of Biotechnology Research Associate
626 fellowship (DBTRA/2023 24/N/JNU/118) from the Government of India.

627 **Funding sources and disclosure of conflicts of interest**

628 The authors declare that the funding source(s) had no role in the study design, data collection,
629 analyses, and interpretation, and in the decision to submit the article for publication. The authors also
630 declare that they have no competing interests related to this manuscript.

631 **Data availability**

The authors declare that the source data supporting the findings of this study are available within the paper and the associated supplementary information files (Supplementary Figures 1-4).

Materials & Correspondence

Correspondence and material requests should be addressed to Souvik Bhattacharjee (*souvik@jnu.ac.in*)

Figure and figure legends

Fig. 1

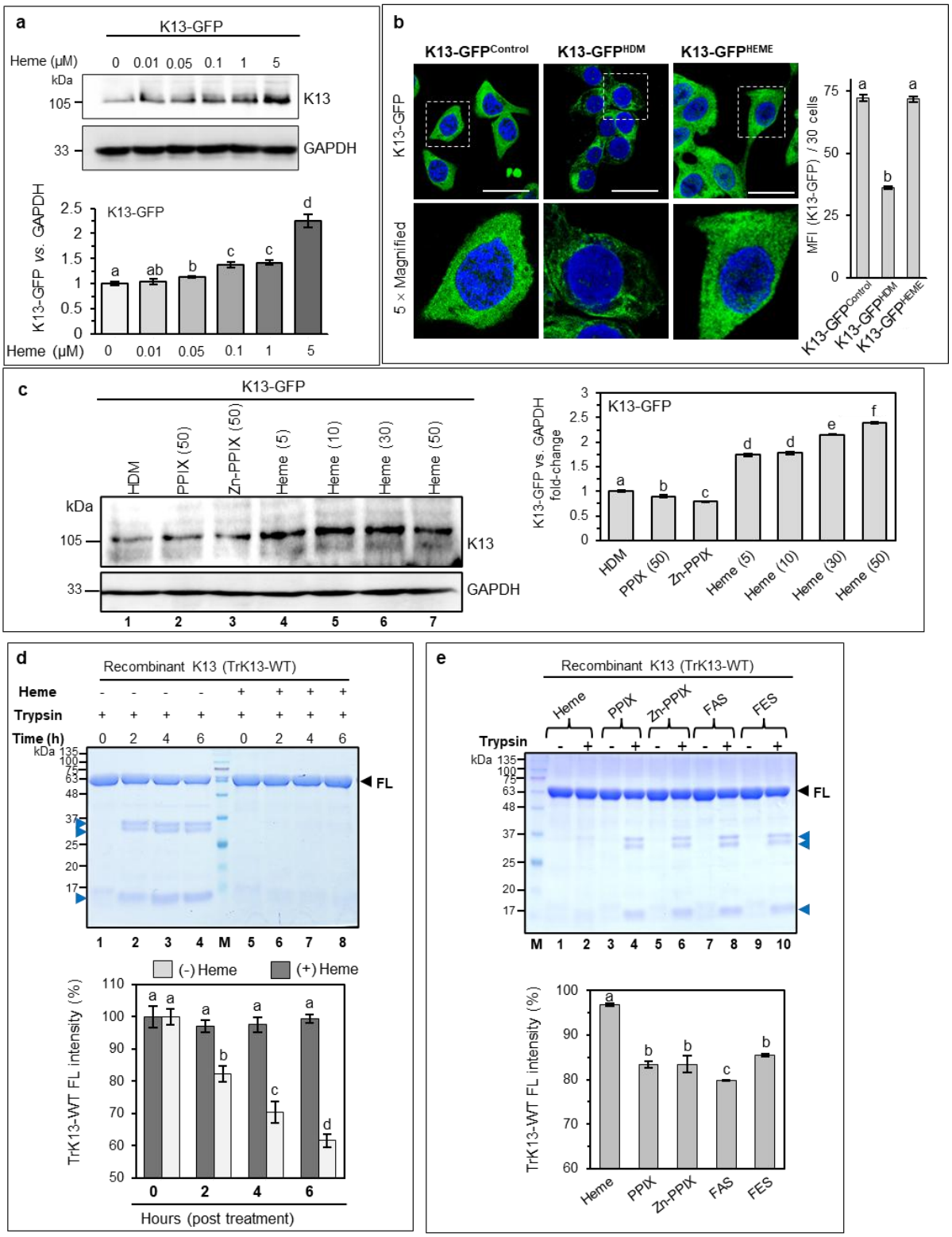

Fig. 1. Heme stabilizes K13-GFP and confers *in vitro* resistance to trypsin digestion. a. Western blots (top) and densitometric analysis (bottom) for K13-GFP under HDM condition or when supplemented with increasing concentrations of heme. GAPDH is the loading control. **b.** IFA images

643 (left) and mean fluorescence intensity plot (MFI, right) of K13-GFP cells under control, HDM or 5 μM
644 heme-supplemented conditions. Scale bar, 5 μm. **c.** Western blot (left) and quantitative densitometric
645 analysis (right) of K13-GFP band intensity under HDM condition (lane 1), or upon supplementation
646 with heme analogs PPIX (lane 2), Zn-PPIX (lane 3) or increasing concentrations (μM) of heme (lanes
647 4-7). Values in parenthesis indicate concentrations (in μM). **d.** Coomassie-stained SDS-PAGE
648 showing trypsin-digested fragments (blue arrowheads) derived from the full length (FL, black
649 arrowhead) recombinant K13 (TrK13-WT) in heme-free (lanes 2-4) and heme-bound TrK13-WT (lanes
650 6-8) protein. The heme-free and heme-bound TrK13-WT protein without trypsin treatment are shown
651 in lanes 1 and 5, respectively. **e.** Coomassie-stained SDS-PAGE showing trypsin-digested fragments
652 (blue arrowheads) derived from the recombinant FL TrK13-WT protein (black arrowhead) when
653 preincubated with heme analogs PPIX, Zn-PPIX, FAS or FES (lanes 4, 6, 8 and 10, respectively) and
654 not by the heme-bound TrK13-WT (lane 2) protein. Lanes 1, 3, 5, 7 and 9 represent samples with no
655 trypsin treatment. Molecular weight standards (M) for all SDS-PAGE and western blots (in kDa) are as
656 indicated. Graphs represent mean from three biological replicates ± SE. Statistical significance
657 calculated by one-way Anova. Distinct alphabets represent significant difference at p.adj ≤ 0.05.

Fig. 2

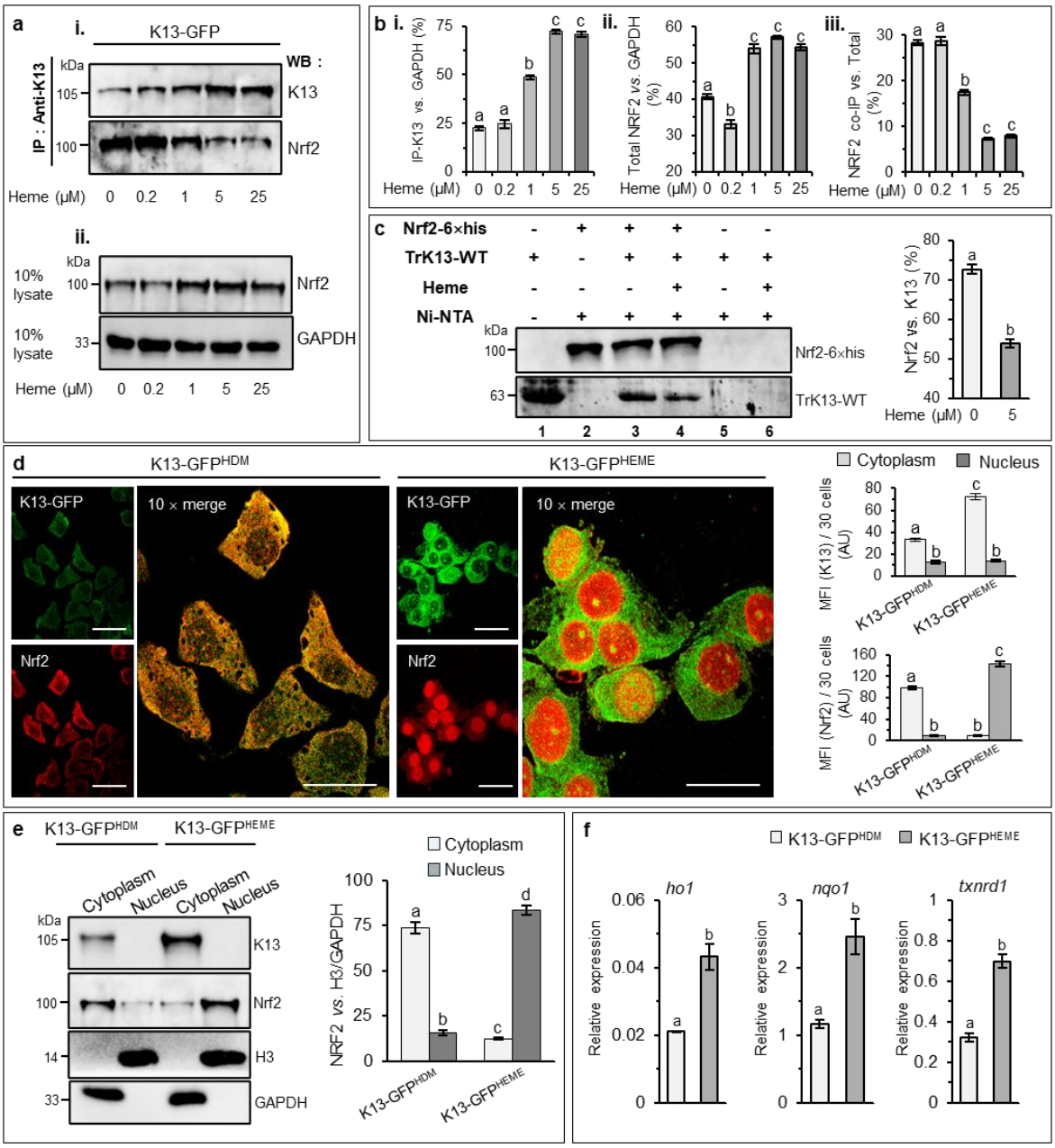

Fig. 2. Heme alters the level and dynamics of the redox reporter Nrf2 in K13-GFP-expressing cells. a. i. Western blots showing immunoprecipitated K13-GFP (top) and the co-associated Nrf2 (bottom) protein from K13-GFP cells cultured in HDM or in the presence of different concentrations of heme. **ii.** Total Nrf2 (top) and GAPDH (bottom, as loading control) in the cellular lysates for conditions in a. **b.** Graphical densitometric analyses of K13-GFP, total Nrf2 and co-purified Nrf2 for data shown in a. **c.** Western blots (left) and graphical densitometric analysis (right) showing reduced co-purification of the heme-bound (lane 4) recombinant K13 (TrK13-WT) by the recombinant Nrf2-6×his

666 protein (pre-bound to Ni-NTA beads) as compared to the heme-free TrK13-WT protein (lane 3) .
667 Lanes 1 and 2 indicate TrK13-WT input and the Ni-NTA bound Nrf2-6×his protein, respectively. Lanes
668 5 and 6 show no nonspecific binding of heme-free or heme-bound TrK13-WT protein to the Ni-NTA
669 beads, respectively. **d.** IFA images showing increased levels of K13-GFP (green) fluorescence and
670 nuclear localization of Nrf2 (red; right panel) in the K13-GFP^{HEME} cells (right). In K13-GFP^{HDM} cells
671 (right), the Nrf2 fluorescence distribution was predominantly cytoplasmic. Scale bar, 5 μm. **e.**
672 Western blots and graphical densitometric quantitation for cytoplasmic and nuclear fractionation of
673 Nrf2 in K13-GFP^{HDM} and K13-GFP^{HEME} cells. **f.** RT-qPCR data showing relative expression of stress-
674 response genes in K13-GFP^{HDM} cells and K13-GFP^{HEME} cells. Molecular weight (in kDa) are as
675 indicated. Error bars represent mean of three technical replicates ± SE. Statistical significance was
676 calculated by one-way Anova. Distinct alphabets represent significant difference at p.adj ≤ 0.05.

Fig. 3

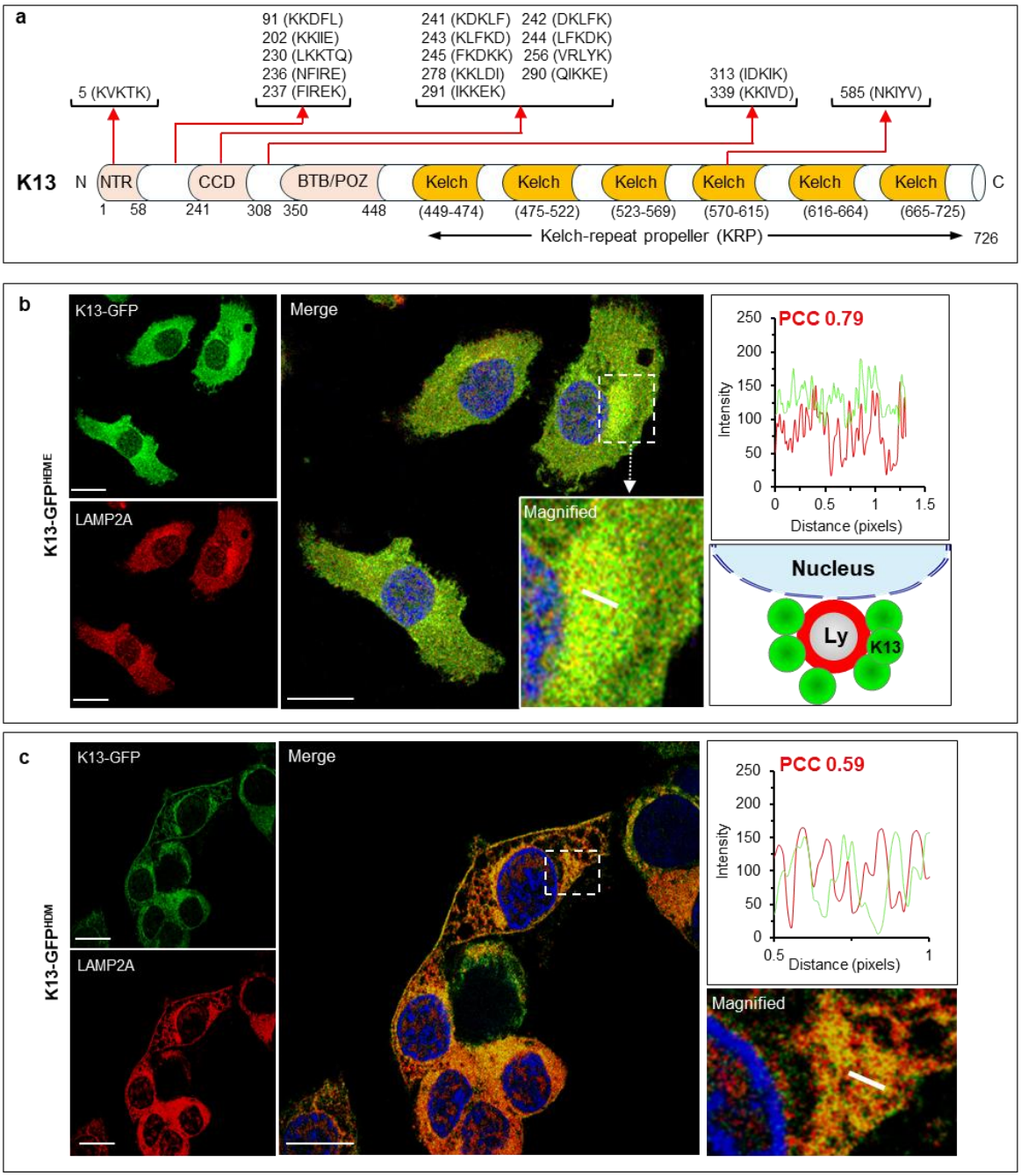

677

678 **Fig. 3. Signature motifs of autophagy in K13 and heme-dependent co-association with**
679 **LAMP2A. a.** Schematic showing the distribution of 18 putative KFERQ-like motifs in different domains
680 of K13, as identified by KFERQ finder v0.8 (*https://rshine.einsteinmed.edu*). NTR, N-terminus domain;
681 CCD, coiled-coil domain; BTB-POZ, Broad-complex, tramtrack and bric-a-brac (BTB)-poxvirus and
682 zinc-finger (POZ) domain. **b-c.** IFA images (left) and RGB intensity plots (right) showing the extent of
683 colocalization between K13-GFP (green) and LAMP2A (red) in K13-GFP^{HDM} (b) and K13-GFP^{HEME}

684 cells (c). Pearson's correlation coefficient (PCC) values for the selected region (white bar) is indicated
685 in red text. Magnified image of the white-dotted boxed region for respective cell is also shown.
686 Schematic in b represents proposed association of K13 with lysosomes based on the inset
687 magnification. Scale bar, 5 μm is shown at the bottom of each image. Cell nucleus (blue) stained with
688 Hoechst 33342.

689

690

Fig. 4

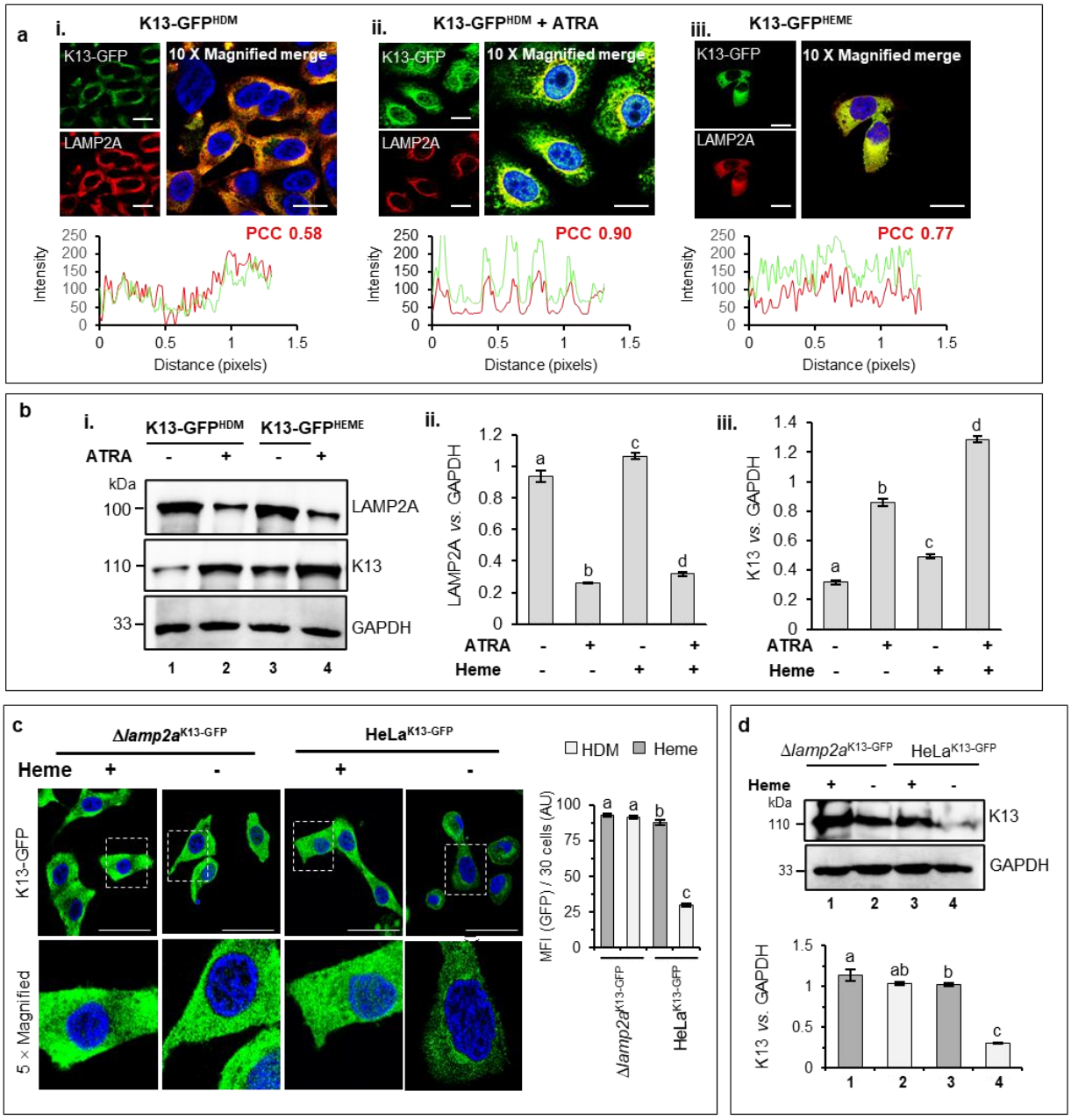

691

692 **Fig. 4. Reduction or knockout of LAMP2A decreases degradation of K13-GFP under HDM**
693 **conditions. a.** In Du145 cells, IFA images and RGB intensity plots (with PCC values) showing relative
694 colocalization between K13-GFP (green) and LAMP2A (red) in K13-GFP^{HDM} cells in the absence (i) or
695 presence (ii) of ATRA (inhibitor of LAMP2A expression) compared to K13-GFP^{HEME} cells (iii).
696 Corresponding fluorescence and merged images were acquired under identical optics and exposure

697 conditions. **b.** Western blots (i) and fold change (ii-iii) for LAMP2A (top), K13-GFP (middle) in the
698 absence or presence of ATRA in cells expressing K13-GFP^{HDM} (lanes 1-2) or K13-GFP^{HEME} (lanes 3-
699 4). GAPDH (bottom) was the loading control. **c.** In HeLa cells, IFA images (left), and graphical MFI
700 (right) of K13-GFP fluorescence (green) in transgenic *Δlamp2a*$^{K13\text{-}GFP}$ and parental HeLa$^{K13\text{-}GFP}$ cells
701 under HDM (-) or heme-supplemented (+) conditions. **d.** Western blots (top) and graphical fold
702 change of K13-GFP (top) in transgenic *Δlamp2a*$^{K13\text{-}GFP}$ (lanes 1-2) and parental HeLa (lanes 3-4) cells
703 under HDM (lanes 2 and 4) or heme-supplemented (lanes 1 and 3) conditions. GAPDH was the
704 loading control. Scale bar for IFA images, 5 μm. Boxed (white dotted) images are magnified in sub-
705 panel. For all statistical analyses, each bar denotes the mean from three technical replicates ± SE.
706 Statistical significance was calculated by one-way Anova. Distinct alphabets represent difference at
707 p.adj ≤ 0.05. Molecular weight (in kDa) for all blots are as indicated.

Fig. 5

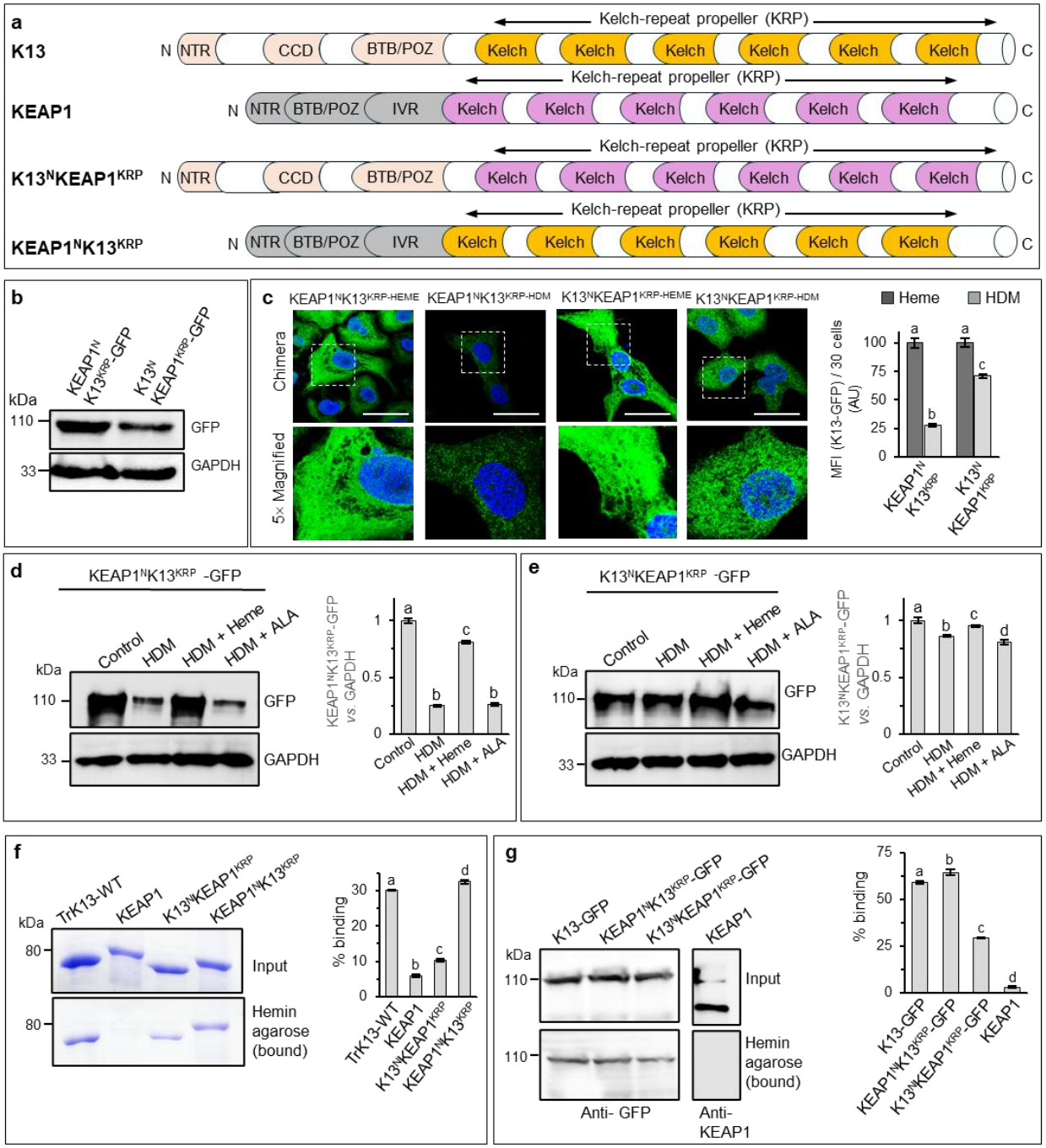

708

709 **Fig. 5. The K13 KRP domain confers heme-dependent stability and heme-binding**
710 **characteristics to KEAP1. a.** Schematics for domain organization in K13, KEAP1, K13^{N}KEAP1^{KRP}
711 and KEAP1^{N}K13^{KRP} chimeric proteins. NTR, N-terminus domain; CCD, coiled-coil domain; BTB-POZ,
712 Broad-complex, tramtrack and bric-a-brac (BTB)-poxvirus and zinc-finger (POZ) domain; IVR,
713 intervening region. **b.** Western blot detecting K13^{N}KEAP1^{KRP}-GFP and KEAP1^{N}K13^{KRP}-GFP
714 (arrowhead) chimeras in transgenic Du145 cells. Loading control is GAPDH. **c.** IFA images and mean

715 fluorescence intensity (MFI) of K13^{N}KEAP1^{KRP}-GFP and KEAP1^{N}K13^{KRP}-GFP cells cultured under
716 HDM or heme-repleted conditions. Nuclei stained with Hoechst 33342 (blue), scale bar, 5 µm.
717 Respective boxed (white dotted) regions are magnified and shown below. **d-e.** Western blots (left)
718 and densitometric fold change (right) in KEAP1^{N}K13^{KRP}-GFP (d) and K13^{N}KEAP1^{KRP} (e) protein band
719 intensities under HDM, heme-repleted or heme precursor aminolevulinic acid (ALA)-containing HDM
720 conditions. **f-g.** Coomassie-stained SDS-PAGE (f) and western blots (g) showing hemin agarose
721 binding by indicated KEAP1-K13 recombinant proteins or chimeras (f) or from respective transgenic
722 Du145 cellular lysates (g). Percentage binding (as compared to the total input) is shown graphically.
723 Molecular weights (in kDa) for SDS-PAGE and western blots are as indicated. Error bars in the
724 graphs represent mean of three technical replicates ± SE. Statistical significance was calculated by
725 one-way Anova. Distinct alphabets represent significant difference at p.adj ≤ 0.05.

Fig. 6

a i.

Transgenic Du145 cell line	IC_{50} (μM)		% change in IC_{50}
	HDM	HEME (5 μM)	
GFP	117.7 ± 0.9	114.7 ± 0.5	2.6 ± 0.7 %
K13-GFP	109.7 ± 0.2	93.8 ± 0.4	18.2 ± 0.6 %
KEAP1	87.8 ± 0.2	83.9 ± 0.8	6.1 ± 1.4 %
$KEAP1^{N}K13^{KRP}$-GFP	102.3 ± 0.3	84.8 ± 0.9	23.7 ± 1.4 %
$K13^{N}KEAP1^{KRP}$-GFP	80.8 ± 0.1	73.9 ± 0.9	13.5 ± 1.8 %

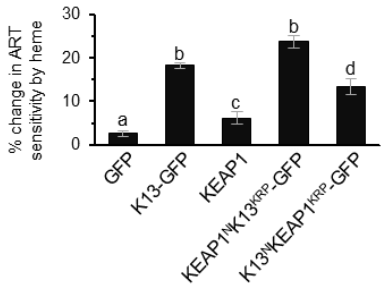

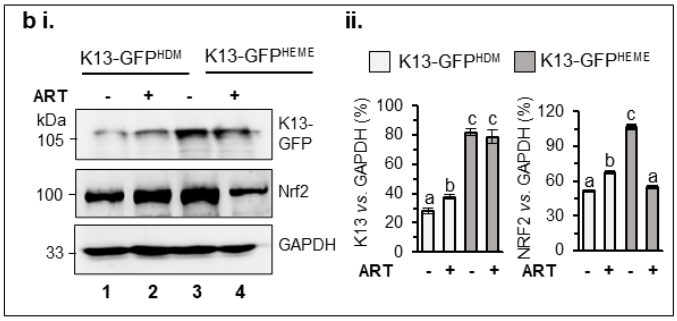

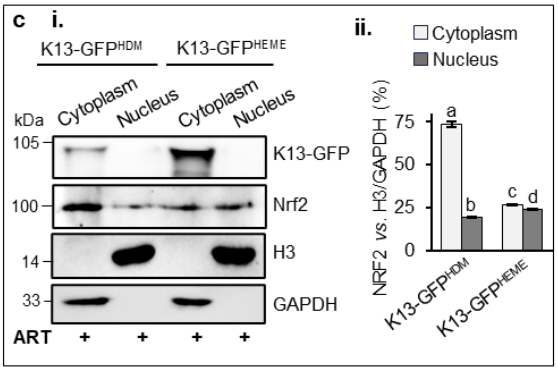

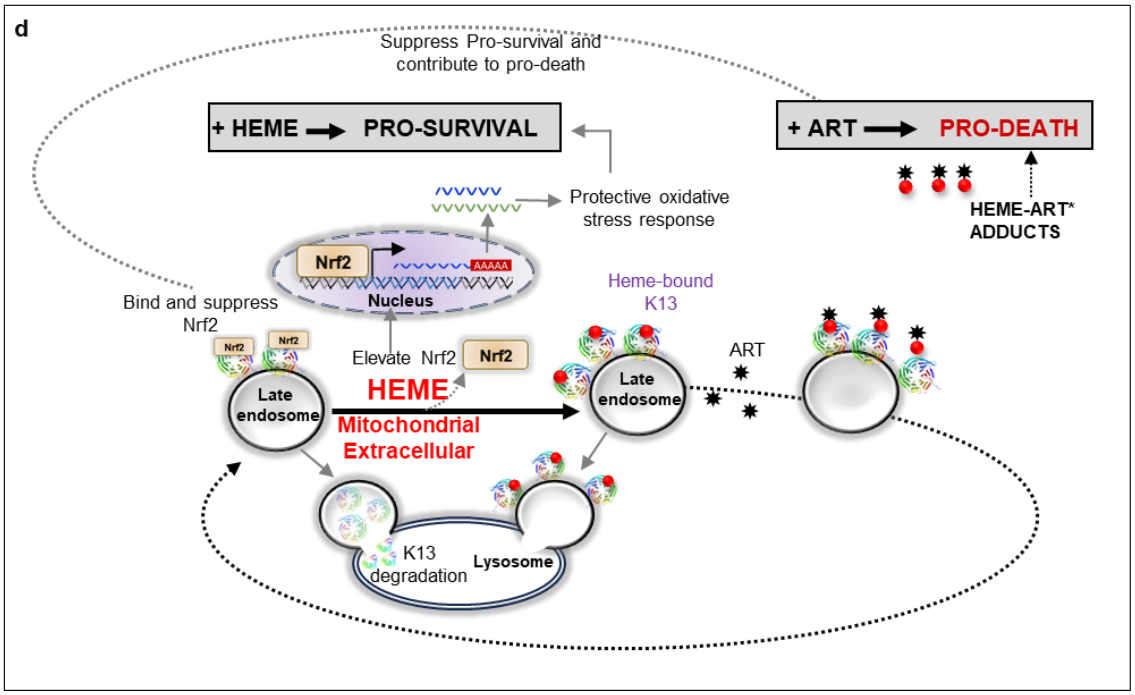

Fig. 6. Dynamics of heme, Nrf2, ART and redox sensitivity in Du145 cells expressing K13. a. IC_{50} values (μM, i) and change in percentage sensitivity to ART (right, ii) in respective transgenic Du145 cell lines on supplementation with 5 μM heme. **b.** Western blots (i) and quantitative densitometric analysis (versus GAPDH, ii) for K13-GFP (top) and Nrf2 (middle) in K13-GFP^{HDM} (lanes

731 1 and 2) and K13-GFP^{HEME} (lanes 3 and 4) cells in the absence (lanes 1 and 3) or presence (lanes 2
732 and 4) of ART. GAPDH (bottom) is the loading control. **c.** Western blots (i) and graphical
733 densitometric quantitation (ii) for cytoplasmic and nuclear fractionation of K13-GFP and Nrf2 in K13-
734 GFP^{HDM} and K13-GFP^{HEME} cells in the presence of ART. Molecular weight (in kDa) are as indicated.
735 Error bars in a-c represent mean of three technical replicates ± SE. Statistical significance was
736 calculated by one-way Anova. Distinct alphabets represent significant difference at p.adj ≤ 0.05. **d.**
737 Model for dynamics of Nrf2 binding by free K13, its displacement by heme and K13-heme mediated
738 activation of ART to induce (i) a pro-survival and (ii) pro-death responses in K13-expressing Du145
739 cells.

740

Fig. 7

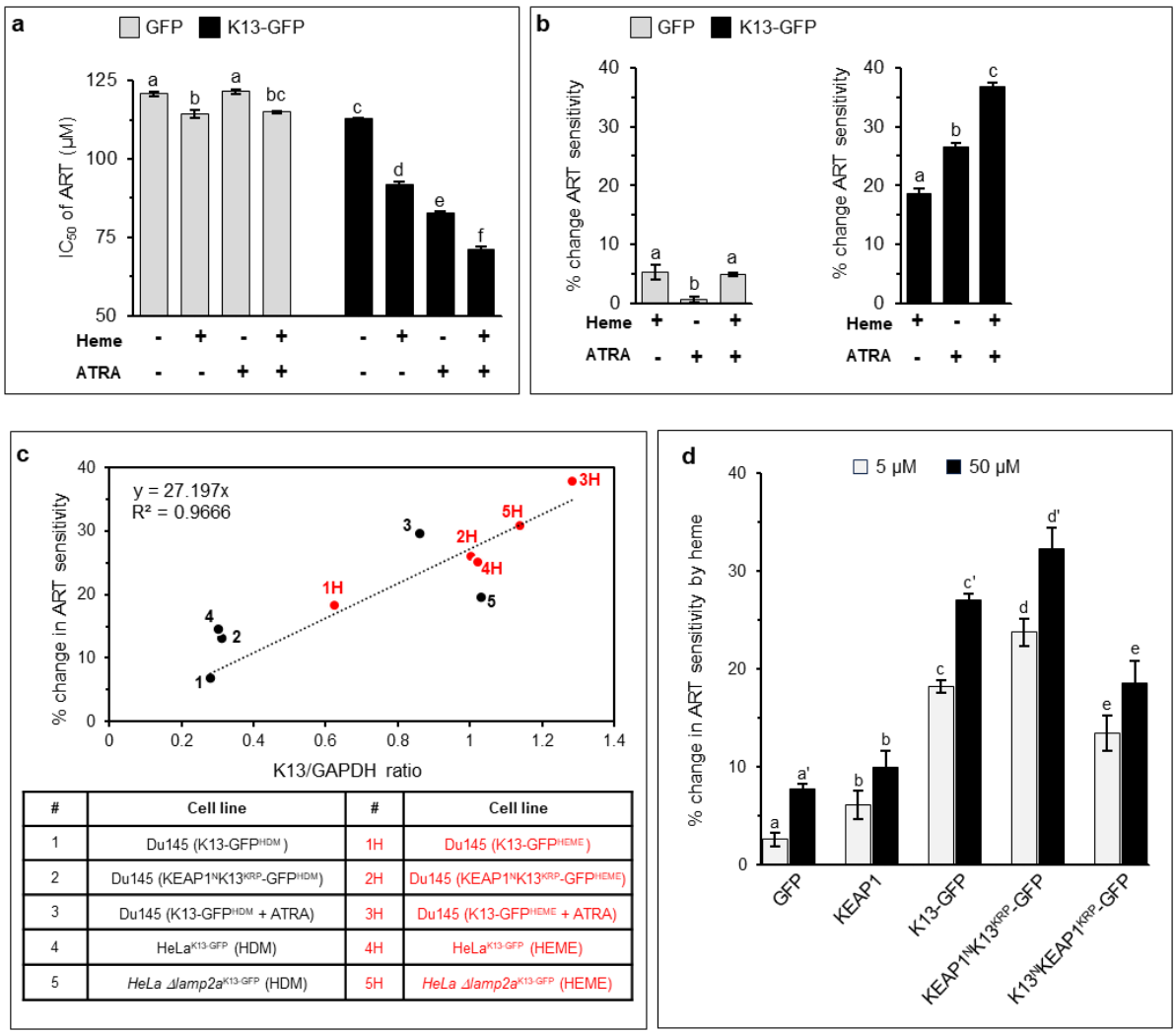

#	Cell line	#	Cell line
1	Du145 (K13-GFP^{HDM})	1H	Du145 (K13-GFP^{HEME})
2	Du145 (KEAP1^{N}K13^{KRP}-GFP^{HDM})	2H	Du145 (KEAP1^{N}K13^{KRP}-GFP^{HEME})
3	Du145 (K13-GFP^{HDM} + ATRA)	3H	Du145 (K13-GFP^{HEME} + ATRA)
4	HeLa$^{K13\text{-}GFP}$ (HDM)	4H	HeLa$^{K13\text{-}GFP}$ (HEME)
5	*HeLa Δlamp2a*$^{K13\text{-}GFP}$ (HDM)	5H	*HeLa Δlamp2a*$^{K13\text{-}GFP}$ (HEME)

Fig. 7. ART sensitivity is increased proportional to K13 intensity. a. IC_{50} values (μM) for GFP and K13-GFP cells in presence or absence of ATRA or heme (5 μM). **b.** Effect of heme (5 μM) and ATRA on percentage change in ART sensitivity in cells expressing GFP (grey bars) or K13-GFP (black bars). **c.** Graph showing the percentage change in ART sensitivity as a function of K13/GAPDH intensity ratio under HDM (solid black circles) or 5 μM heme-repleted (solid red circles) conditions in transgenic Du145 and HeLa cells. Black dotted trendline and R-squared values are indicated. Description of cells is shown at the bottom. Numbers only and numbers followed by initial 'H' indicate cells cultured under HDM or 5 μM heme-repleted conditions, respectively. **d.** Graph showing change in percentage sensitivity to ART at extracellular 5 μM (grey) and 50 μM (black) heme in the repleted media. Error bars in a, b and d represent mean of three technical replicates ± SE. Statistical

752 significance was calculated by one-way Anova. Distinct alphabets represent significant difference at

753 p.adj ≤ 0.05.

754

755

Fig. 8

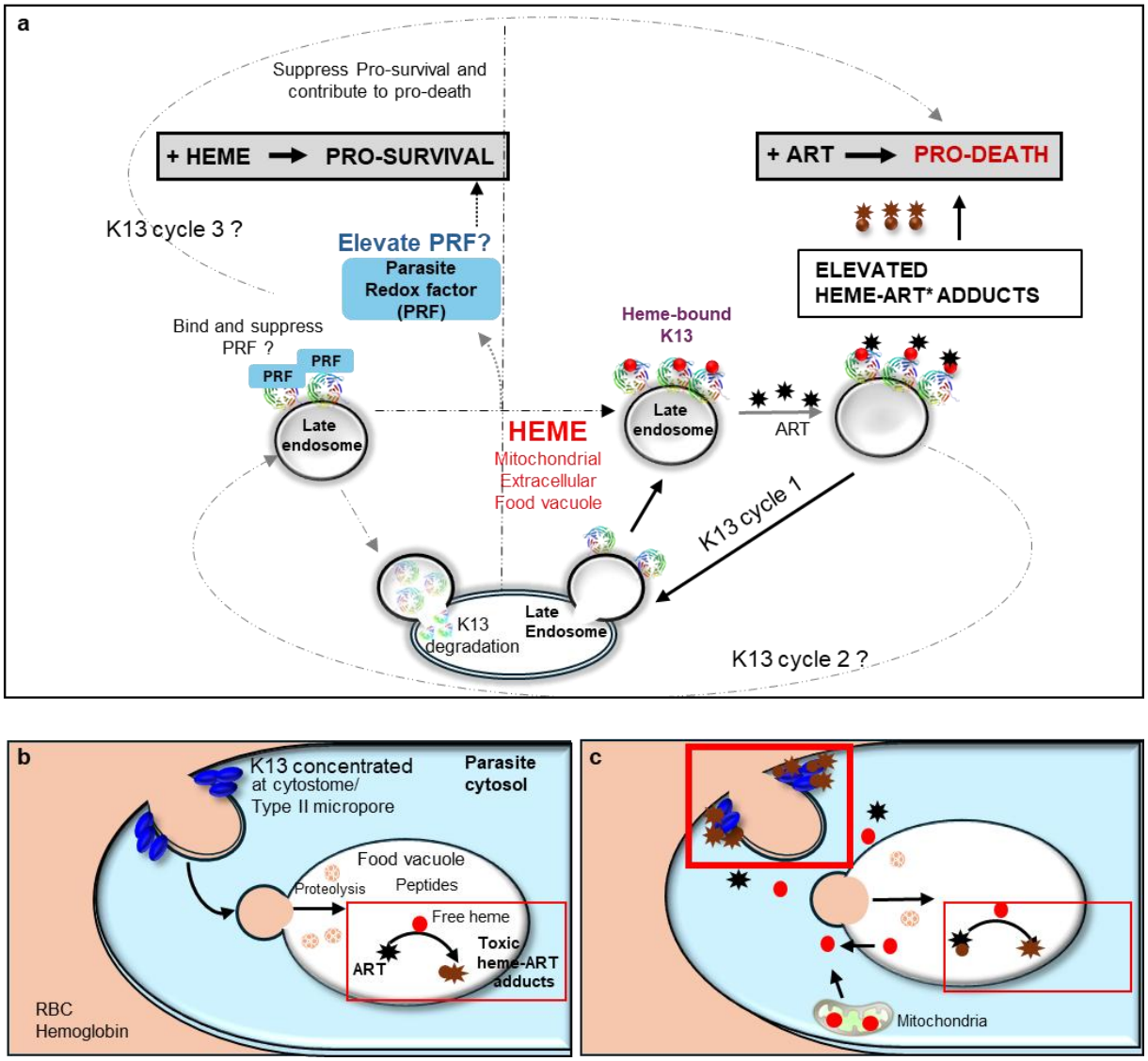

756

757 **Fig. 8. Models for K13-heme binding and ART activation with implications for *P. falciparum.* a.**
758 ART induced pro-death mechanisms and their possible modulation in rings and trophozoites. Our
759 primary conclusion is for **K13 in cycle 1** (bold lines), where K13 binds heme and becomes stabilized
760 at cytoplasmic face of endosomal (Type I, rings; or Type II, trophozoites) micropore membranes. For
761 both stages, heme may come from mitochondrial and extracellular sources, while in trophozoites, the
762 food vacuole may also contribute. K13-heme activates (ART*) to heme-ART* adducts, which
763 dissociate from K13 and whose toxicity to a wide range of cellular targets, triggers a pro-death
764 response in the parasite. Heme-free K13 may re-cycle back to resume heme binding and re-initiate

765 cycle 1 and reinforce death outcomes. **K13 cycle 2** may be initiated if a (yet hypothetical) parasite
766 redox factor (PRF) binds K13 and becomes suppressed until heme-binding dislodges the PRF to
767 activate ART and pro-death effects, acting additively with cycle 1. **K13 cycle 3** may be initiated upon
768 K13 displacement of PRF to trigger pro-survival responses and reduce pro-death effects of cycles 1
769 and 2. **b-c.** K13-heme is catalytic for ART activation in trophozoites. K13 (dark blue) concentrates at
770 cytostome structures that enable hemoglobin digestion and liberation of free heme (filled red circles)
771 in the food vacuole, b. Existing models propose that free heme (red circle) activates ART (black star)
772 to toxic heme-ART adducts (dark brown hybrid star-circle) in the food vacuole (see red box). In c, we
773 propose that heme (red circles) from the food vacuole and other sources (like the mitochondria)
774 transported to the parasite bind K13 (solid blue spheres) concentrated at the cytostome, which greatly
775 stimulates formation of activated ART (ART*), and toxic heme-ART adducts (brown complexes in bold
776 red box) compared to encounters of ART with free heme in the food vacuole.

777

778 **References**

779 1. Nosten, F. & White, N. J. Artemisinin-based combination treatment of falciparum malaria. *Am.*
780 *J. Trop. Med. Hyg.* **77**, 181–192 (2007).

781 2. Eastman, R. T. & Fidock, D. A. Artemisinin-based combination therapies: A vital tool in efforts
782 to eliminate malaria. *Nature Reviews Microbiology* vol. 7 (2009).

783 3. Meshnick, S. R. Artemisinin: Mechanisms of action, resistance and toxicity. in *International*
784 *Journal for Parasitology* vol. 32 (2002).

785 4. Sutherland, C. J., Henrici, R. C. & Artavanis-Tsakonas, K. Artemisinin susceptibility in the
786 malaria parasite Plasmodium falciparum: propellers, adaptor proteins and the need for cellular
787 healing. *FEMS Microbiol. Rev.* **45**, (2021).

788 5. Ribbiso, K. A. *et al.* Artemisinin-based drugs target the plasmodium falciparum heme
789 detoxification pathway. *Antimicrob. Agents Chemother.* **65**, (2021).

790 6. Zhang, S. & Gerhard, G. S. Heme activates artemisinin more efficiently than hemin, inorganic

791 iron, or hemoglobin. *Bioorganic Med. Chem.* **16**, (2008).

792 7. Rosenthal, M. R. & Ng, C. L. Plasmodium falciparum Artemisinin Resistance: The Effect of
793 Heme, Protein Damage, and Parasite Cell Stress Response. *ACS Infectious Diseases* vol. 6
794 (2020).

795 8. Pires, C. V. *et al.* Oxidative stress changes the effectiveness of artemisinin in Plasmodium
796 falciparum. *MBio* **15**, (2024).

797 9. Zhu, P. & Zhou, B. The Antagonizing Role of Heme in the Antimalarial Function of Artemisinin:
798 Elevating Intracellular Free Heme Negatively Impacts Artemisinin Activity in Plasmodium
799 falciparum. *Molecules* **27**, (2022).

800 10. Rocamora, F. *et al.* Oxidative stress and protein damage responses mediate artemisinin
801 resistance in malaria parasites. *PLoS Pathog* **14**, e1006930 (2018).

802 11. Ariey, F. *et al.* A molecular marker of artemisinin-resistant Plasmodium falciparum malaria.
803 *Nature* **505**, 50–55 (2014).

804 12. Straimer, J. *et al.* Drug resistance. K13-propeller mutations confer artemisinin resistance in
805 Plasmodium falciparum clinical isolates. *Science (80-.).* **347**, 428–431 (2015).

806 13. WHO. World malaria report 2024. *https://www.who.int/teams/global-malaria-*
807 *programme/reports/world-malaria-report-2024* (2024).

808 14. Cui, L., Mharakurwa, S., Ndiaye, D., Rathod, P. K. & Rosenthal, P. J. Antimalarial drug
809 resistance: Literature review and activities and findings of the ICEMR network. *American*
810 *Journal of Tropical Medicine and Hygiene* vol. 93 (2015).

811 15. Menard, D. *et al.* A Worldwide Map of Plasmodium falciparum K13-Propeller Polymorphisms.
812 *N Engl J Med* **374**, 2453–2464 (2016).

813 16. Xie, S. C., Ralph, S. A. & Tilley, L. K13, the Cytostome, and Artemisinin Resistance. *Trends in*
814 *Parasitology* vol. 36 (2020).

815 17. Blasco, B., Leroy, Di. & Fidock, D. A. Antimalarial drug resistance: Linking Plasmodium

816 falciparum parasite biology to the clinic. *Nature Medicine* vol. 23 (2017).

817 18. Fairhurst, R. M. & Dondorp, A. M. Artemisinin-Resistant Plasmodium falciparum Malaria.
818 *Microbiol Spectr* **4**, (2016).

819 19. Bhattacharjee, S. *et al.* Remodeling of the malaria parasite and host human red cell by vesicle
820 amplification that induces artemisinin resistance. *Blood* **131**, 1234–1247 (2018).

821 20. Birnbaum, J. *et al.* A Kelch13-defined endocytosis pathway mediates artemisinin resistance in
822 malaria parasites. *Science (80-.).* **367**, 51–59 (2020).

823 21. Tutor, M. V. *et al.* The Plasmodium falciparum artemisinin resistance-associated protein Kelch
824 13 is required for formation of normal cytostomes. *bioRxiv* (2023).

825 22. Rahman Abdur *et al.* Artemisinin-resistant Plasmodium falciparum Kelch13 mutant proteins
826 display reduced heme-binding affinity and decreased artemisinin activation. *Commun Biol.* **13**,
827 1499 (2024).

828 23. Severance, S. & Hamza, I. Trafficking of heme and porphyrins in metazoa. *Chem. Rev.* **109**,
829 (2009).

830 24. Schultz, I. J., Chen, C., Paw, B. H. & Hamza, I. Iron and porphyrin trafficking in heme
831 biogenesis. *Journal of Biological Chemistry* vol. 285 (2010).

832 25. Ascenzi, P. *et al.* Hemoglobin and heme scavenging. *IUBMB Life* vol. 57 (2005).

833 26. Morgan, W. T., Heng Liem, H., Sutor, R. P. & Muller-Eberhard, U. Transfer of heme from
834 heme-albumin to hemopexin. *BBA - Gen. Subj.* **444**, (1976).

835 27. Yi, L. & Ragsdale, S. W. Evidence that the heme regulatory motifs in heme oxygenase-2 serve
836 as a thiol/disulfide redox switch regulating heme binding. *J. Biol. Chem.* **282**, (2007).

837 28. Gamiz-Arco, G. *et al.* Heme-binding enables allosteric modulation in an ancient TIM-barrel
838 glycosidase. *Nat. Commun.* **12**, (2021).

839 29. Chiabrando, D., Vinchi, F., Fiorito, V., Mercurio, S. & Tolosano, E. Heme in pathophysiology: A

840 matter of scavenging, metabolism and trafficking across cell membranes. *Front. Pharmacol.* **5**,
841 (2014).

842 30. Jiang Tempel W. Loppnau P. Graslund S. He H. Ravichandran M. Seitova A. Arrowsmith C.H.
843 Edwards A.M. Bountra C. El Bakkouri M. Senisterra G. Osman K.T. Lovato D.V. Hui R.
844 Hutchinson A. Lin Y.H., D. Q. Crystal Structure Analysis of Kelch protein from Plasmodium
845 falciparum. *Struct. Genomics Consort.* (2015).

846 31. Li, X., Zhang, D., Hannink, M. & Beamer, L. J. Crystal structure of the Kelch domain of human
847 Keap1. *J. Biol. Chem.* **279**, 54750–54758 (2004).

848 32. Billett, H. H. *Hemoglobin and Hematocrit*. *Clinical Methods: The History, Physical, and*
849 *Laboratory Examinations* (Butterworths, 1990).

850 33. Aich, A., Freundlich, M. & Vekilov, P. G. The free heme concentration in healthy human
851 erythrocytes. *Blood Cells, Mol. Dis.* **55**, (2015).

852 34. Donegan, R. K., Moore, C. M., Hanna, D. A. & Reddi, A. R. Handling heme: The mechanisms
853 underlying the movement of heme within and between cells. *Free Radical Biology and*
854 *Medicine* vol. 133 (2019).

855 35. White, N. J. Anaemia and malaria. *Malaria Journal* vol. 17 (2018).

856 36. Nagaraj, V. A. *et al.* Malaria Parasite-Synthesized Heme Is Essential in the Mosquito and Liver
857 Stages and Complements Host Heme in the Blood Stages of Infection. *PLoS Pathog.* **9**,
858 (2013).

859 37. Ke, H. *et al.* The heme biosynthesis pathway is essential for Plasmodium falciparum
860 development in mosquito stage but not in blood stages. *J. Biol. Chem.* **289**, (2014).

861 38. Abshire, J. R., Rowlands, C. J., Ganesan, S. M., So, P. T. C. & Niles, J. C. Quantification of
862 labile heme in live malaria parasites using a genetically encoded biosensor. *Proc. Natl. Acad.*
863 *Sci. U. S. A.* **114**, (2017).

864 39. Heller, L. E. & Roepe, P. D. Quantification of Free Ferriprotoporphyrin IX Heme and Hemozoin

865 for Artemisinin Sensitive versus Delayed Clearance Phenotype Plasmodium falciparum
866 Malarial Parasites. *Biochemistry* **57**, (2018).

867 40. Stone, K. R., Mickey, D. D., Wunderli, H., Mickey, G. H. & Paulson, D. F. Isolation of a human
868 prostate carcinoma cell line (DU 145). *Int. J. Cancer* **21**, (1978).

869 41. Jayakumar, S., Kunwar, A., Sandur, S. K., Pandey, B. N. & Chaubey, R. C. Differential
870 response of DU145 and PC3 prostate cancer cells to ionizing radiation: Role of reactive
871 oxygen species, GSH and Nrf2 in radiosensitivity. *Biochim. Biophys. Acta - Gen. Subj.* **1840**,
872 (2014).

873 42. Zhang, P. *et al.* Loss of Kelch-like ECH-associated protein 1 function in prostate cancer cells
874 causes chemoresistance and radioresistance and promotes tumor growth. *Mol Cancer Ther* **9**,
875 336–346 (2010).

876 43. Morgan, W. T. & Smith, A. Domain structure of rabbit hemopexin. Isolation and
877 characterization of a heme-binding glycopeptide. *J. Biol. Chem.* **259**, (1984).

878 44. Tolosano, E. & Altruda, F. Hemopexin: Structure, function, and regulation. *DNA and Cell*
879 *Biology* vol. 21 (2002).

880 45. Goel, N. *et al.* Plasmodium falciparum Kelch13 and its artemisinin-resistant mutants assemble
881 as hexamers in solution: a SAXS data-driven modelling study. *FEBS J.* **289**, (2022).

882 46. Makarska-Bialokoz, M. Interactions of hemin with bovine serum albumin and human
883 hemoglobin: A fluorescence quenching study. *Spectrochim. Acta - Part A Mol. Biomol.*
884 *Spectrosc.* **193**, (2018).

885 47. Kensler, T. W., Wakabayashi, N. & Biswal, S. Cell survival responses to environmental
886 stresses via the Keap1-Nrf2-ARE pathway. *Annual Review of Pharmacology and Toxicology*
887 vol. 47 (2007).

888 48. Mense, S. M. & Zhang, L. Heme: A versatile signaling molecule controlling the activities of
889 diverse regulators ranging from transcription factors to MAP kinases. *Cell Research* vol. 16
890 (2006).

891 49. Taguchi, K. *et al.* Keap1 degradation by autophagy for the maintenance of redox homeostasis.
892 *Proc. Natl. Acad. Sci. U. S. A.* **109**, (2012).

893 50. Kirchner, P. *et al.* Proteome-wide analysis of chaperone-mediated autophagy targeting motifs.
894 *PLoS Biol.* **17**, (2019).

895 51. Agarraberes, F. A. & Dice, J. F. A molecular chaperone complex at the lysosomal membrane
896 is required for protein translocation. *J. Cell Sci.* **114**, (2001).

897 52. Stricher, F., Macri, C., Ruff, M. & Muller, S. HSPA8/HSC70 chaperone protein. *Autophagy* **9**,
898 (2013).

899 53. Ikami, Y., Terasawa, K., Watabe, T., Yokoyama, S. & Hara-Yokoyama, M. The two-domain
900 architecture of LAMP2A within the lysosomal lumen regulates its interaction with
901 HSPA8/Hsc70. *Autophagy Reports* vol. 1 (2022).

902 54. Zhu, L. *et al.* Chaperone-mediated autophagy degrades Keap1 and promotes Nrf2-mediated
903 antioxidative response. *Aging Cell* **21**, (2022).

904 55. Anguiano, J. *et al.* Chemical modulation of chaperone-mediated autophagy by retinoic acid
905 derivatives. *Nat. Chem. Biol.* **9**, (2013).

906 56. Probst, B. L., McCauley, L., Trevino, I., Wigley, W. C. & Ferguson, D. A. Cancer cell growth is
907 differentially affected by constitutive activation of NRF2 by KEAP1 deletion and
908 pharmacological activation of NRF2 by the synthetic triterpenoid, RTA 405. *PLoS One* **10**,
909 (2015).

910 57. Gnadig, N. F. *et al.* Insights into the intracellular localization, protein associations and
911 artemisinin resistance properties of Plasmodium falciparum K13. *PLoS Pathog* **16**, e1008482
912 (2020).

913 58. Siddiqui, G., Srivastava, A., Russell, A. S. & Creek, D. J. Multi-omics Based Identification of
914 Specific Biochemical Changes Associated With PfKelch13-Mutant Artemisinin-Resistant
915 Plasmodium falciparum. *J Infect Dis* **215**, 1435–1444 (2017).

916 59. Atul *et al.* Artemisinin resistance in P. falciparum: Probing the interacting partners of Kelch13
917 protein in parasite. *J. Glob. Antimicrob. Resist.* (2023) doi:10.1016/j.jgar.2023.08.012.

918 60. Wang, J. *et al.* Haem-activated promiscuous targeting of artemisinin in Plasmodium
919 falciparum. *Nat Commun* **6**, 10111 (2015).

920 61. Gao, P. *et al.* Profiling the Antimalarial Mechanism of Artemisinin by Identifying Crucial Target
921 Proteins. *Engineering* (2023) doi:10.1016/j.eng.2023.06.001.

922 62. Harding, C. R. *et al.* Genetic screens reveal a central role for heme metabolism in artemisinin
923 susceptibility. *Nat Commun* **11**, 4813 (2020).

924 63. Wan, W. *et al.* The Toxoplasma micropore mediates endocytosis for selective nutrient salvage
925 from host cell compartments. *Nat. Commun.* **14**, (2023).

926 64. Haldar, K. & Bhattacharjee, S. Vesicular mechanisms of drug resistance in apicomplexan
927 parasites. *Microbiol. Mol. Biol. Rev.* **89**, 1–17 (2025).

928 65. Sinai, A. P. & Roepe, P. D. Autophagy in Apicomplexa: a life sustaining death mechanism?
929 *Trends Parasitol* **28**, 358–364 (2012).

930 66. Ghosh, D., Walton, J. L., Roepe, P. D. & Sinai, A. P. Autophagy is a cell death mechanism in
931 Toxoplasma gondii. *Cell. Microbiol.* **14**, (2012).

932 67. Suzuki, K., Bose, P., Leong-Quong, R. Y., Fujita, D. J. & Riabowol, K. REAP: A two minute cell
933 fractionation method. *BMC Res. Notes* **3**, (2010).

934